

Development and validation of CAE based methodology to study sloshing of liquid in an automotive fuel tank

Atul Jadhav
(ME13M1029)

A Dissertation Submitted to
Indian Institute of Technology Hyderabad
In Partial Fulfillment of the Requirements for
The Degree of Master of Technology



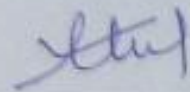
भारतीय प्रौद्योगिकी संस्थान हैदराबाद
Indian Institute of Technology Hyderabad

Department of Mechanical and Aerospace Engineering

June, 2015

Declaration

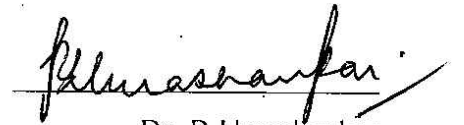
I declare that this written submission represents my ideas in my own words, and where others' ideas or words have been included, I have adequately cited and referenced the original sources. I also declare that I have adhered to all principles of academic honesty and integrity and have not misrepresented or fabricated or falsified any idea/data/fact/source in my submission. I understand that any violation of the above will be a cause for disciplinary action by the Institute and can also evoke penal action from the sources that have thus not been properly cited, or from whom proper permission has not been taken when needed.



Atul Jadhav
(ME13M1029)

Approval Sheet

This thesis entitled “Development and validation of CAE based methodology to study sloshing of liquid in an automotive Fuel Tank” by Atul Jadhav is approved for the degree of Master of Technology from IIT Hyderabad.



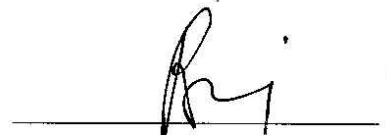
Dr. B Umashankar

Assistant Professor,

Department of Civil Engineering,

Indian Institute of Technology, Hyderabad

Examiner



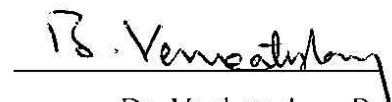
Dr. Raja Banerjee

Associate Professor,

Department of Mechanical and Aerospace Engineering,

Indian Institute of Technology, Hyderabad

Adviser



Dr. Venkatesham B.

Assistant Professor,

Department of Mechanical and Aerospace Engineering,

Indian Institute of Technology, Hyderabad

Co-Adviser

Acknowledgements

The work presented here would not have been possible without the guidance and support of many people who in one way or the other extended their valuable assistance. I take this opportunity to express my sincere gratitude towards them.

First and foremost, I express my deep gratitude to my guide Dr. Raja Banerjee for offering me a challenging project like this, reposing confidence that this would be executable by me in the given time frame, and providing valuable guidance, professional advice, thoughtful suggestions and mature conduct.

A very special thanks to Dr. Venkatesham B, for his continuous support, suggestions and thoughtful interventions at all stages of the project.

I would like to thank each and every faculty of my department for their guidance throughout my course work.

I would like to thank Mercedes-Benz Research & Development India, for giving me opportunity to work on real world problem and financial support for my project.

I mention my deep thankfulness to my project colleague Mayur Kothari for supporting and helping me throughout the project.

I extend my thanks to all my lab mates Anil, Rakesh, Ashwani, Vatsalya for their support in my work. I am very much thankful to my dear friends Shweta, Deepsikha, Sarang and Sukanya for their support and making my stay in IITH one of the most memorable ones. I am also thankful to each and every member of IIT Hyderabad who had been supportive throughout my stay here for the last two years.

Dedicated to

My Family

Abstract

Due to advancement in automobile technology, various types of automobile noises have been reduced significantly and hence sloshing noise has become a major irritant for passengers. Past studies have concluded that the slosh noise is directly connected with the pressure fluctuation dp/dt which in turn can be provided by CFD study of flow dynamics of working fluid in the fuel tank. The present work includes experimental and CFD study of flow dynamics of working fluid in a rectangular tank on Reciprocating Test Setup (RTS). Experiments have been performed on indigenously developed Reciprocating Test Setup (RTS). Experiments were conducted with varying fill level, sensor location and excitation frequency. The inertial acceleration from experiment has been taken as input for CFD analysis. Commercial CFD solver STAR CCM+ was used to perform the CFD simulations dynamic pressure, wave height and Particle Image Velocimetry (PIV) validation has been done to compare the CFD results with experiments.

Contents

Declaration.....	ii
Approval Sheet.....	iii
Acknowledgements	iv
Abstract	vi
1 Introduction	1
1.1 Sloshing.....	1
1.2 Literature Review.....	4
1.3: Objective.....	5
2 Experimental Setup	6
2.1 Overview.....	6
2.2 Subsystem Details.....	7
3 Particle Image Velocimetry.....	12
3.1 Introduction.....	12
3.2 Working principle of PIV	13
3.3 Particle Image Velocimetry	14
3.4 Experimental Setup	15
3.5 Thumb Rules for PIV Analysis	21
3.6 Interrogation and cross correlation of PIV images.....	25
3.7 Experimental Procedure	28
4 Numerical Model.....	30
4.1 Numerical Modelling.....	30
4.2 Numerical Formulation.....	34

5 Results and Discussion	40
5.1 Experimental Results	40
5.2 CFD Analysis	45
5.3 Wave Height Comparison.....	47
5.4 Dynamic Pressure comparison between CFD and Experiment.....	52
5.5 PIV Analysis	62
6 Conclusion and Future work	68
7 References	70

Chapter 1

Introduction

1.1 Sloshing

Sloshing refers to any motion of the free liquid surface inside its container. It is caused by any disturbance to partially filled liquid containers. Depending on the type of disturbance and container shape, the free liquid surface can experience different types of motion including simple planar, nonplanar, rotational and chaotic motions. Sloshing of liquids within closed containers thus represents one of the most fundamental fluid-structure interaction problem and has been the subject of many industrial studies like Liquefied Natural Gas (LNG) carriers and their new design, rockets and airplanes fuel reservoirs and road tankers over the past few decades.

The basic problem of liquid sloshing involves the estimation of hydrodynamic pressure distribution, forces, and natural frequencies of the free-liquid surface. These parameters have a direct effect on the dynamic stability and performance of moving containers.

The problem of liquid sloshing in moving or stationary containers remains of great concern to aerospace, civil, and nuclear engineers, physicists, designers of road tankers and ship tankers, and automotive industry. Civil engineers have been studying liquid sloshing effects on large dams, oil tanks and elevated water towers under ground motion to check the stability of structure under violent liquid motions. The problem of liquid sloshing dynamics has been of major concern to aerospace engineers studying the influence of liquid propellant sloshing on the flight performance of jet vehicles and its stability. Instabilities in flight characteristics can result if fuel slosh frequency becomes close to any of the sub-system frequencies. The dynamic stability of liquefied natural gas tankers and ship cargo tankers, and liquid hydrodynamic impact loading are problems of current interest to the designers of such systems. In populated cities, gasoline and other flammable liquid tankers are prone to rollover accidents while entering and exiting highways.

Liquid sloshing in automotive applications creates a large variety of problems of practical safety importance, including tank trucks on highways, and liquid cargo in oceangoing vessels. In populated cities, gasoline and other flammable liquid tankers are prone to rollover accidents while entering and exiting highways. This is a difficult mathematical problem to solve analytically, since the dynamic boundary condition at the free surface is nonlinear and the position of the free surface varies with time in a manner not known a priori. Analytical solutions are limited to regular geometric tank shapes, such as cylindrical and rectangular. The nature of sloshing dynamics in cylindrical tanks is better understood than for prismatic tanks. However, analytical techniques for predicting large-amplitude sloshing are still not fully developed. Such loads are extremely important in the design stage of supporting structure and internal components of vehicle tanks. In addition, much of the sloshing technology developed for space applications is not applicable to automotive industry. The reason is that more emphasis has been placed on frequencies and total forces as they relate to control requirements. Accordingly, the effects of local peak impact pressure on structural requirements have not been studied to any extent. Further, the excitation amplitudes considered in space applications are too small for road vehicle simulation. To avoid catastrophic sloshing in space vehicles, the control system frequencies, the vehicle elastic structure frequencies, and the fluid-slosh frequencies must be fairly widely separated.

The requirements for high perceived quality and quietness in vehicles have become stricter in recent years. In addition, the development period for new vehicles is becoming increasingly shorter. Currently, new fuel tanks are mainly being developed on the basis of bench tests and vehicle driving tests conducted using actual tanks but no definitive design method has been established yet, a great deal of time is required to address the issue of fuel sloshing noise. Due to the modifications in automotive technologies, slosh noise originating from motion of fuel within the tank, is a typical annoyance that may emerge above the ambient background noise during low speed conditions or parking. The sloshing noise problem becomes more significant as the customer's expectation of a quiet automobile gets higher. Therefore, the current research tries to develop a CAE based methodology to predict slosh noise in an automotive fuel tank.

Fuel Tank sloshing noise is categorized as shown below:

- **Low-frequency Noise Resulting from Vibration**

This noise occurs when fuel moves to one side of the tank and strongly strikes the inner wall due to the force exerted on it by vehicle braking. The vibration that occurs in the tank is mainly transferred as solid-borne vibration that is heard as sloshing noise in the interior. This is also called as Hit noise (Fig 1.1) in which wave front hits the tank wall and transmission of noise depends on acoustical properties of tank wall. This is the dominant source of noise inside fuel tanks.

- **High-frequency Air-borne Noise**

When a vehicle stops following braking, this noise occurs as a result of rippling fuel replacing air in convex portions of the tank design. It is mainly transmitted as air-borne noise that penetrates the interior. It is classified into splash noise (Fig 1.2) and clonk noise (Fig 1.3) where there is fluid-fluid interaction.

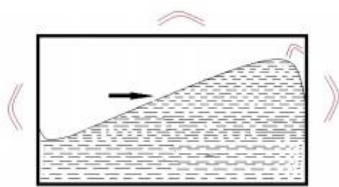


Figure 1.1 Hit Noise

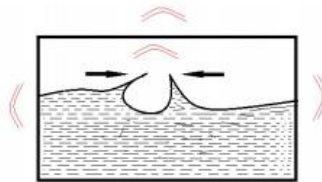


Figure 1.2 Splash Noise

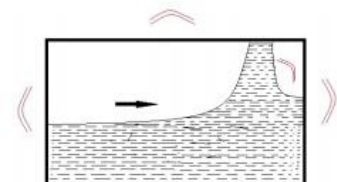


Figure 1.3 Clonk Noise

Sloshing noise also depends on the mounting of fuel tank inside the vehicle. If a tank is mounted with its maximum dimension facing in the direction of motion of vehicle, then wave has to travel a large distance before reaching the wall and then it hits the wall giving rise to hitting noise with less splashing. On the other hand, if maximum dimension facing in the perpendicular to motion of vehicle, so that the distance between the two walls is less, so wave smoothly climbs up the wall hits the top surface of tank and splashes giving rise to splashing noise.

1.2 Literature Review

Thiagrajan et al.[1] worked on sloshing in a rectangular tank using sway excitation and observed that 20% and 80% fill level causes higher pressure than other conditions. Wachowski [2] et.al classified sloshing noise in hit noise, splash noise and clonk noise and depends upon the fill level, excitation and tank geometry. Wiesche [3] derived a correlation between slosh noise pressure fluctuations within the sloshing liquid. He used two-phase Computational Fluid Dynamics (CFD) to track liquid interface within realistic tank geometries to determine these pressure fluctuations. He discussed effect of anti-slosh element (Baffles and pads) on the slosh dynamics. However prediction about the absolute sound level cannot be made. Vytla and Ando [4] studied uni-directional fluid structure interaction simulation of a fuel tank sloshing on an actual fuel tank geometry using commercial codes and concluded that lower fill levels have higher potential to generate sloshing noise. Peric and Zorn [5] studied the structural impact of sloshing loads caused by quantified various nonlinear factors that affect the performance, stability and structural integrity of the tanks and floating vessels.

Hattori et al [6] studied different types of waves generated due to sloshing and classified them on the basis of impact pressure pattern achieved during experimentation with a specific type of wave. Ibrahim [7] provides a comprehensive review of linear and nonlinear inviscid theoretical methods for sloshing in various geometries, along with the compilation of published experimental data.

Khezzar et al.[8] studied sloshing in rectangular tank subjected to impulsive force and concluded that flow visualization of experimental and numerical simulation were similar. Rezaei et al. [9] developed a numerical code for sloshing and validated their results from experiments performed by Hinatsu et al.[10] The above two studies have concluded that flow dynamics can be efficiently captured in numerical simulation and is comparable to flow visualization recorded during experiments.

Lugni et al [11] studied the event of “flip through” that takes place during impact of wave on a vertical wall and its effect on dynamic pressure at the wall. R Banerjee et al.[12] studied the effect of various turbulence models and concluded that k- ϵ model predicts the flow component of velocity well.

1.3 Objective

The research work documented here is a part of a research effort dedicated for the development of a CAE (Computer Aided Engineering) based methodology to study sloshing phenomenon inside automotive fuel tank. Previously work has been done on Impact Test Setup (ITS) [13][14] which replicates actual vehicle condition. It was found that all the three regimes of sloshing i.e. Impact regime, Transition Regime, Linear Regime occurs in a single run of experiment. So to study these regimes separately, Reciprocating Test Setup (RTS) is developed to have better control on excitation frequency.

This work includes CFD study of flow dynamics of working fluid (water) inside the tank. Inertial acceleration data from experiment is the input to CFD study and dynamic pressure on tank walls is calculated at predefined locations on tank wall. The output of this study i.e. dynamic pressure will be the input for structural and acoustic study to predict sloshing noise.

The first part of this work includes description of experimental setup for Reciprocating Test Setup (RTS) and procedure used to carry out experimentation study. PIV study to predict velocity vectors inside the rectangular tank on RTS setup is also included. The second part includes CFD based numerical procedure used for analysis. It includes formulation of numerical models and focuses on interface tracking method used.

The third part is dedicated to results analysis which includes efficacy of numerical procedure using mesh independence study and effect of various turbulence models. Reciprocating Test setup experimental results that include inertial acceleration, dynamic pressure, velocity contours and image correlation at some crank angle is carried out. Wave height as well as dynamic pressure validation has been done between CFD and experiments for various cases. Velocity vectors calculated from experiment is compared with CFD and analytical formula in linear and weakly nonlinear sloshing regime. Parametric study is carried out by varying fill level and excitation frequency to study sloshing phenomenon in linear, weakly nonlinear and nonlinear sloshing regime.

Chapter 2

Experimental Setup

2.1 Overview

The schematic diagram of the Reciprocating test rig (RTS), which simulates the sloshing phenomenon under controlled excitation to measure dynamic pressure, dynamic force and dynamic acceleration on the tank wall is shown in figure 2.1. The system consists of four major subsystems which are servo motor with multi turn potentiometer, coupling disc which connects the motor shaft to the connecting rod and on which there is provision for variation of amplitude of excitation, base plate with bearings attached at bottom moving on guide bars and rectangular tank with provision for sensor mounting.

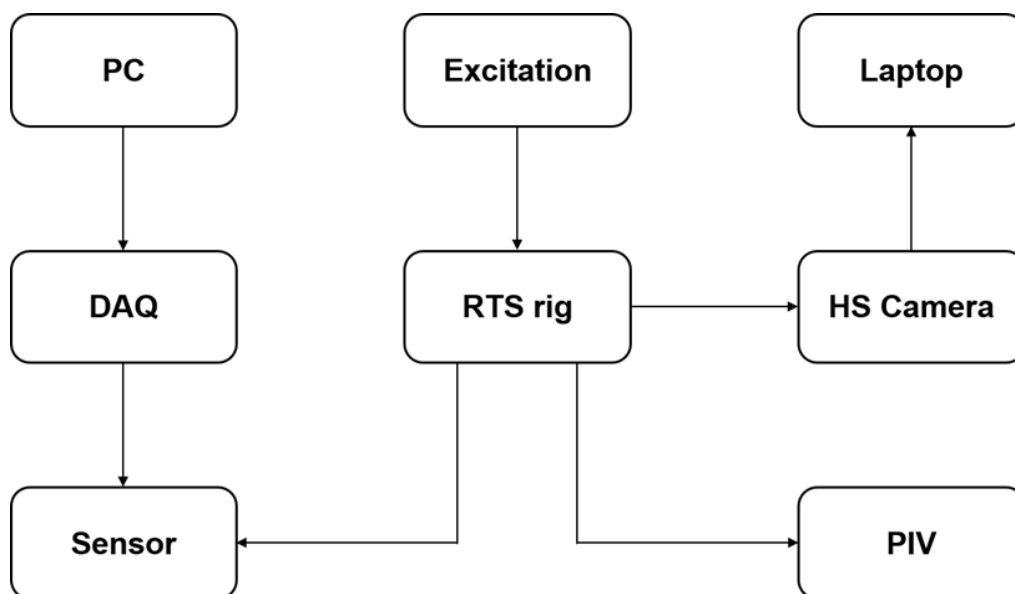
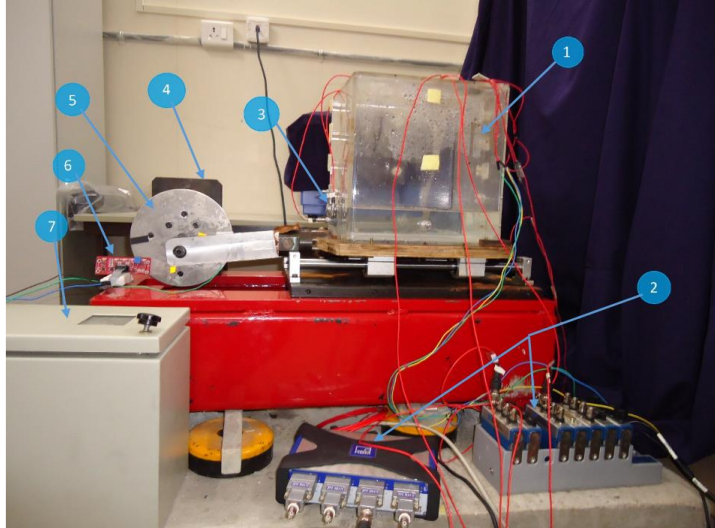


Figure 2.1: Schematic Diagram of Reciprocating Test Setup (RTS)



1. Rectangular tank with integration of sensor mounting
2. Data Acquisition System (HBM and NI DAQ)
3. Dynamic Sensors: Dynamic Pressure sensor, Dynamic acceleration sensor, Dynamic force sensor
4. Connecting Disk
5. Line sensor
6. Multi turn potentiometer

Figure 2.2: Experimental Setup

Figure 2.2 shows the experimental setup for Reciprocating Test Rig. The subsystems involved in it are as follows:

2.2 Subsystem details

❖ Rectangular tank with integration of sensors mounting

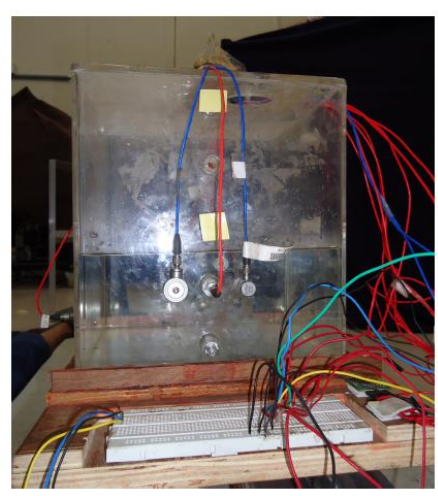


Figure 2.3: Acrylic tank with sensor mountings

Figure. 2.3 shows, a transparent rectangular tank made of Acrylic was fabricated with a length of 238 mm, width of 220 mm and height of 238mm. The tank wall was 6 mm thick. This tank was placed over a wooden platform that was attached to quieter wheels in order to reduce background noise. The platform was maintained at a horizontal position with respect to the ground with the help of a spirit level.

A three axis linear inertia acceleration sensor (Figure 2.3 (a)) (3g-ADXL335) and a line triggering sensor were mounted on this platform. The inertia sensor is used to monitor vehicle acceleration and deceleration. Depending on the experimental condition, the sensors can be mounted at 10 %, 30 %, 50 % and 70 % of tank height.

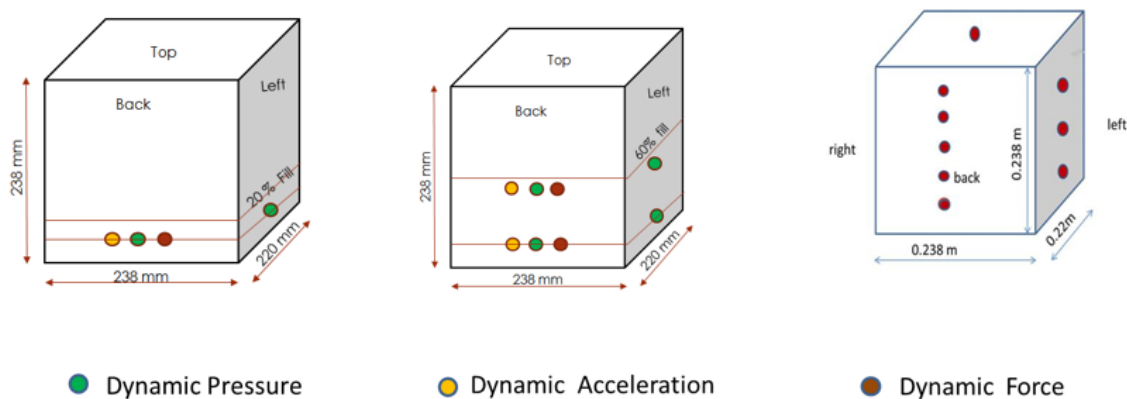


Figure 2.4: Schematic diagram of sensor mounting locations (a) 20 % fill (b) 60 % fill

Figure 2.4 shows, sensor mounting location for 20 % fill and 60 % fill level. Most of the dynamic action is observed mostly in front and back wall of tank, so dynamic force and dynamic acceleration sensors are mounted on those walls. As fluid comes directly in contact with dynamic pressure sensor, so to capture dynamic events at the wall, dynamic pressure sensors are mounted on front, back and right wall of the tank. As the lateral movement of the tank is avoided, so the same dynamic events can be captured in left and right sensors (so only one dynamic pressure sensor is enough). Sloshing is surface wave phenomenon, to capture this sensor location is fixed at 10 % below fill level. For example, suppose fill level is 60 % then the sensor height should be chosen as 50 % , sensors are also kept at constant 10 % height to see behavior change at different

fluid layers. At each sensor height position, dynamic pressure is mounted at center and dynamic force and dynamic acceleration sensors are mounted besides to the dynamic pressure sensor.

❖ Sensors integration with Data Acquisition



Figure 2.5: Data acquisition system

HBM Quantum X DAQ is used to capture dynamic pressure on tank wall which was triggered by the line sensor, which is in turn was activated by the color change in the vehicle track. It's a NI cDAQ-9178 data acquisition system.

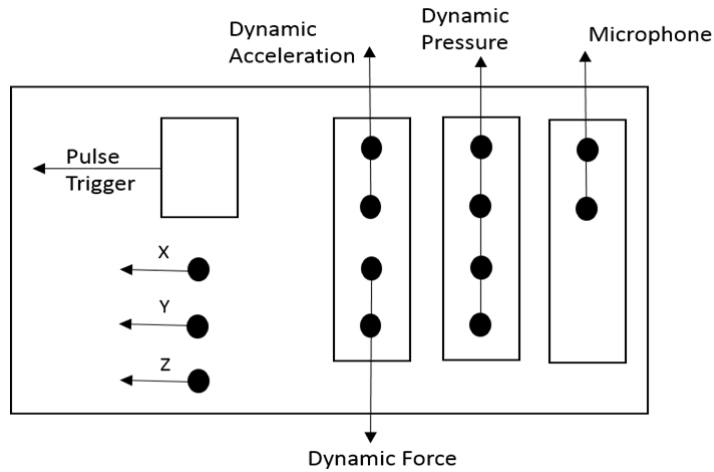


Figure 2.6: Schematic diagram of Data Acquisition system

Figure 2.6 schematic diagram of DAQ is being used as interface between sensors and LabView software. Data from all sensors were acquired using a NI cDAQ-9178 data acquisition system which was triggered by the line sensor, which is in turn was activated by the color change in the vehicle track. A customized Labview program was used to acquire the data from all the sensors. Code extended to all the sensors and a way to synchronize the data from these sensors is been established.

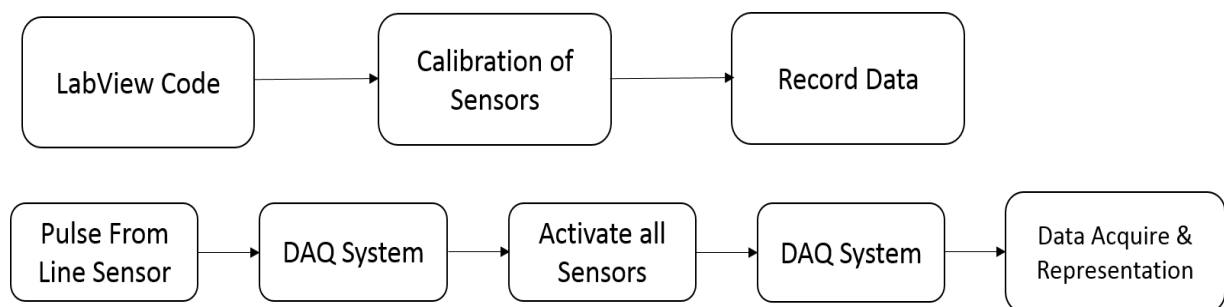


Figure 2.7: Schematic diagram of data acquisition process

Dynamic pressure sensors: Figure 2.8 (b) shows, dynamic pressure sensor. Dytran 2300 V3 model is used to measure dynamic pressure at specified locations on the wall of the tank. Sensitivity of the sensor is 10 mV/PSI. Dynamic force sensors: Figure. 2.8 (c) shows, dynamic force sensor. Dytran 1053V3 and Dytran 1051V4 models used to measure dynamic force on the wall of the tank. Sensitivity of the sensor used was 11.24 mV/N. Dynamic acceleration sensors

Figure 2.8 (d) shows the dynamic acceleration sensor. Dytran 3055B1 with sensitivity 10 mV/g. is used to measure the dynamic acceleration on wall.



Figure 3.8: Sensors used for data acquisition (a) Inertial acceleration sensor (b) Dynamic pressure sensor (c) Dynamic force sensor (d) Dynamic acceleration sensor (e) High speed camera

High speed camera

Figure. 2.8 (e) shows high speed camera- Phantom V12.1, used to capture the sloshing events inside the tank. 1000 fps frame rate was used to capture small sloshing moments. Camera is also triggered with rest of the sensors to make it possible to compare all the data with respect to the time frame.

Depending on the experimental condition, the sensors can be mounted at 10 %, 30 % and 50 % of tank height as shown in Figure 2.4. An extensive study was conducted to determine repeatability of the test data. Parametric studies were conducted with varying fill levels and sensor locations.

Sr. No.	Fill Level	Excitation Frequency	Sensor Location
1	20%	0.5fs, 0.75fs, 1fs	10%
2	40%	0.5fs, 0.6fs, 1fs	10%, 30%
3	60%	0.5fs, 0.85fs, 1fs	10%, 50%

Chapter 3

Particle Image Velocimetry (PIV)

3.1 Introduction

Particle image velocimetry (PIV) is an established optical diagnostic technique that effectively samples the velocity of a given fluid within a flow field. PIV records the position over time of small tracer particles introduced into the flow to extract the local fluid velocity. Thus, PIV represents a quantitative extension of the qualitative flow visualization techniques that have been practiced for several decades. The main aim of the present study is to get the instantaneous velocity vectors of particles so as to define the motion of fluid inside the tank.

Violent water free-surface motions under gravity are of concern in many engineering applications. In the context of coastal engineering, the impact of steep water waves can result in damage or collapse of structures. With reference to the naval context, when the energy of the ship motion is sufficiently large in the frequency domain close to the lowest natural tank mode, violent sloshing phenomena can be excited. In all the conditions mentioned, extremely high impact pressures can be measured that largely exceed those associated with the internal pressure of the waves. Recorded pressures are of the order of 10–100 times the hydrostatic pressure associated with the impacting wave height, depending on the impact conditions. Also air cushioning of wave impacts causes pressures significantly greater than atmospheric, by the contraction of air pocket leading to increased pressure maxima. This clearly suggests that the largest pressures are essentially due to the flow inertia, gravity effects being negligible. The shape of the impacting wave has a significant effect on wave impact pressure exerted on vertical walls. However, because of the experimental difficulties associated with recording the details of the impact for reliable recording of impact pressure peaks, this study focuses on flow visualization techniques where one can define flow characteristics in terms of velocity vectors.

3.2 Working principle of PIV

The tracer particles are added to the flow which are illuminated by a laser sheet in a plane of the flow at least twice within a short time interval. The light scattered by the particles is recorded on a sequence of frames. The displacement of the particle images between the light pulses is determined through evaluation of the PIV recordings. In order to be able to handle the great amount of data which can be collected employing the PIV technique, sophisticated post-processing is required. Figure 3.1 briefly sketches a typical setup for PIV recording. Small tracer particles are added to the flow. A plane (light sheet) within the flow is illuminated twice by means of a laser (the time delay between pulses depending on the mean flow velocity and the magnification at imaging). It is assumed that the tracer particles move with local flow velocity between the two illuminations. The light scattered by the tracer particles is recorded by camera. For evaluation the digital PIV recording is divided in small subareas called “interrogation areas”. The local displacement vector for the images of the tracer particles of the first and second illumination is determined for each interrogation area by means of statistical methods. It is assumed that all particles within one interrogation area have moved homogeneously between the two illuminations. The projection of the vector of the local flow velocity into the plane of the light sheet (two-component velocity vector) is calculated taking into account the time delay between two illuminations.

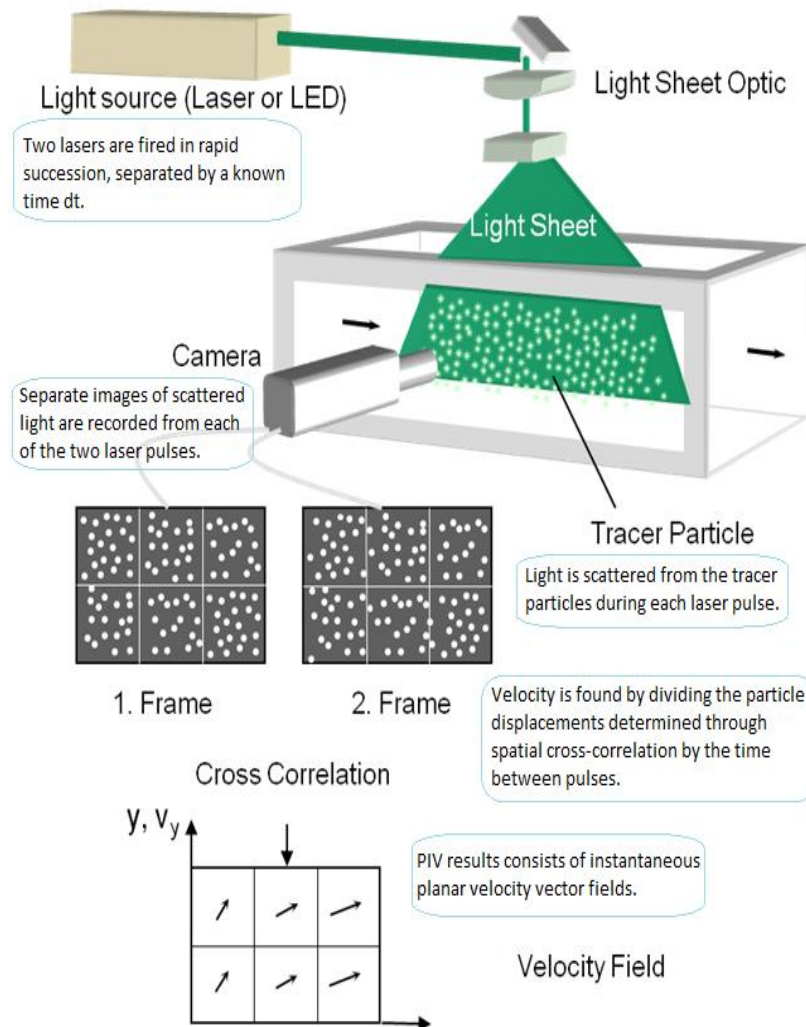


Figure 3.1: Schematic diagram of PIV setup

3.3 Particle Image Velocimetry

3.3.1 Seeding

To visualize flow for PIV purposes, the fluid has to be seeded with particles. To follow the flow accurately, these particles need to be neutrally buoyant and small with respect to the flow phenomena studied. Seeding the flow with light reflecting particles is necessary in order to image the flow field. The particles should be small enough to follow the flow but large enough to

reflect the required amount of light. A good rule of thumb is that around ten particles should be correlated for each measured velocity vector.

3.3.2 Illumination

In PIV flow studies, illumination is usually provided by a laser light sheet. A narrow sheet of light is used to define the plane of investigation. It prevents blurry imaged particles just above or below the focused plane, which would pollute the PIV images and thereby adversely affect the analysis result. A laser is used because it can deliver a bright sheet with almost constant thickness without aberration or diffusion, due to the coherent and monochromatic character of the emitted light. The slightly diverging light beam produced by a laser is usually transformed into a sheet by converging it with a weak positive lens and subsequently make the beam fan out in one plane to a sheet by an additional cylindrical lens. This results in a sheet with a slightly converging thickness, to select a certain sheet thickness tuned to the experimental conditions.

For the PIV study, Nano and LPY series of pulsed Nd:YAG lasers are used.

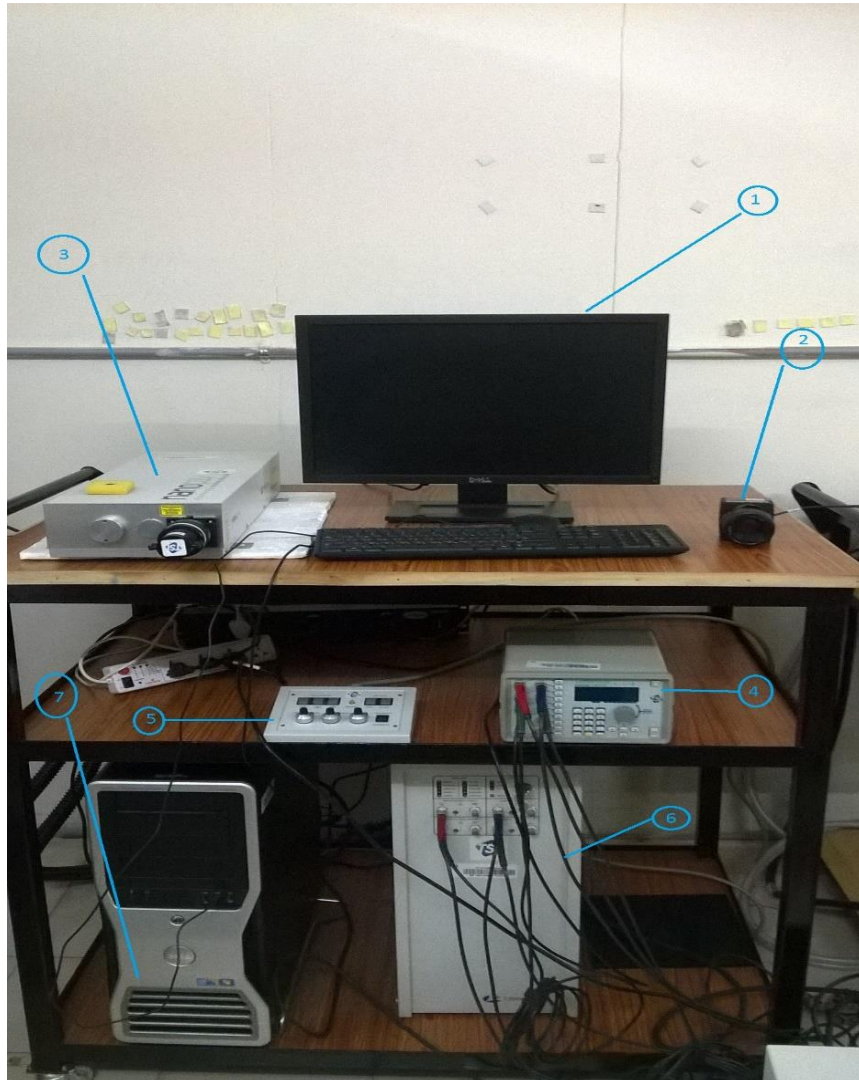
3.3.3 Imaging

The illuminated plane in the particle seeded flow is imaged by a camera with its optical axis perpendicular to the plane, in order to record the whole plane in focus. High quality lenses are generally necessary because the light levels are usually relatively low and large apertures have to be used.

3.4 Experimental Setup

The experimental setup of a PIV system typically consists of several subsystems.

Figure 3.2 shows the experimental setup for Particle Image Velocimetry. The subsystems involved in it are as follows:



1. Computer
2. Camera
3. Litron Laser
4. Synchronizer
5. Control Box
6. PIV Unit
7. CPU

Figure 3.2 : Experimental setup of PIV

3.4.1 Subsystem Details:

3.4.1.1 Camera

The Model 630059 POWERVIEW™ Plus 4MP PIV Camera is used for Particle Image Velocimetry (PIV) measurements. It is provided with a Progressive Scan Interline CCD imaging device with minimum frame straddling time for PIV capture of 200 ns. The camera captures particle images from the illuminated flow field for the measurement of the velocities in the flow field. Two modes of operations are offered in the camera. The Free-Run mode is used for the

alignment and diagnostic of the system, while the Frame Straddling mode is employed for actual flow field measurements. When the images are captured using the Frame Straddling mode from the camera, the images are analyzed using the cross-correlation technique to calculate the velocity flow fields.

PIV measurements require sufficient laser light sheet intensity to get good exposures of the small seed particles used to follow the fluid flow. When the laser intensity is high enough to give near full-scale intensity levels for the particle images, but below pixel saturation, damage to the camera CCD array can happen if a specular reflection goes into the camera. Specular reflections can be caused by objects in the flow like the flow model, and by droplets and bubbles. If the laser damage threshold is exceeded within the image area, a pixel or group of pixels may be damaged. The pixel damage can be seen as white pixels when the lens cap is on. For that purpose, 532 nm filter is used for measurement to save camera lens.

Camera is provided with two modes of operation:

Free Run Mode:

For alignment and initial diagnostics of the PIV system, the camera can be operated in Free-Run mode. In Free-Run mode there is no synchronization between the laser and camera.

Frame Straddling Mode:

The Frame Straddling mode is used when PIV images are acquired for the actual flow field measurements. The control of the Frame Straddling mode is performed in the INSIGHT software. When the camera is set at the Frame Straddling mode, the camera takes two consecutive image frames as one image capture. The timing separation between the laser exposures in these two consecutive images is determined by the Delta T set in the INSIGHT software. The Delta T is the time separation between the two laser pulses to illuminate the flow field. The appropriate Delta T is set dependent upon the velocity magnitude of the flow field being measured.

3.4.1.2 Litron Laser

For PIV setup, lasers are predominant due to their ability to produce high-power light beams with short pulse durations. This yields short exposure times for each frame. Nd:YAG lasers, used in PIV setup, emit primarily at 1064 nm wavelength and its harmonics (532, 266, etc.).

The laser optics consist of a spherical lens and cylindrical lens combination. The cylindrical lens expands the laser into a plane while the spherical lens compresses the plane into a thin sheet. This is critical as the PIV technique cannot generally measure motion normal to the laser sheet and so ideally this is eliminated by maintaining an entirely 2-dimensional laser sheet. It should be noted though that the spherical lens cannot compress the laser sheet into an actual 2-dimensional plane. The minimum thickness is on the order of the wavelength of the laser light and occurs at a finite distance from the optics setup (the focal point of the spherical lens). This is the ideal location to place the analysis area of the experiment.

Laser Timing Diagram:

Figure 3.3 shows the laser timing diagram. The blue line represents the triggering device, when it goes down, the sequence begins. The green vertical lines represent laser pulses, and the red line represents the camera exposures; when the red line is up, the camera exposure is on, when the line is down, the exposure has stopped. There are 2 camera exposures, and that the 2 laser pulses "straddle" the interframe time between the 2 camera exposures. This is referred to as "frame-straddling."

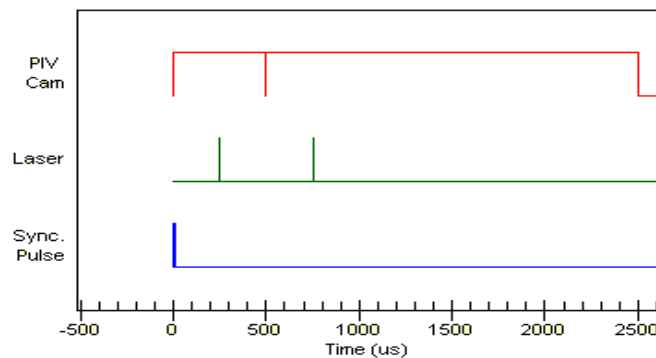


Figure 3.3 : Laser Timing Diagram

Laser Pulse Delay : Pulse delay time is the amount of time to wait from the start of a pulse sequence to until the first laser pulse. It is set to 400 μs .

Delta T (μs) : The pulse separation (dT) is the time for which camera is exposed to light. Using time study, it is set to 3000 μs where particle movement can be seen clearly in interrogation window.

PIV Exposure (μs) : It is time that the first frame on your PIV camera(s) is open. It is set to 600 μs .

External Trigger :

Trigger Delay (ms): It is for delaying the camera trigger. It indicates the time from the start of a pulse sequence until the camera is triggered. It is set to 0.

Trigger Timeout (ms): It is the duration of time for which the synchronizer must wait to receive an external trigger input. For current settings, it is 10000 ms.

Laser Pulses / Trigger: It specifies the number of laser pulses per external trigger. For current experiment, it is kept 1 laser pulse/ trigger so as to get 10 frames for 10 laser pulses.

3.4.1.3 Synchronizer

The synchronizer acts as an external trigger for both the camera and the laser. Controlled by a computer, the synchronizer can dictate the timing of each frame of the CCD camera's sequence in conjunction with the firing of the laser to within 1 ns precision. Thus the time between each pulse of the laser and the placement of the laser shot in reference to the camera's timing can be accurately controlled.

3.4.1.4 Control Box

Figure 3.4 shows Control box is used to switch on or off pump and laser and also to open or close shutter. It is also provided with flashlamp and Q-switch controls.

Repetition Rate

This is the frequency at which the flashlamp triggers. On a computer controlled system the actual

repetition rate is entered, but on a manual controlled system the adjustment dial is set so that the maximum repetition rate is achieved when the dial is at the maximum setting. The adjustment is also linear in this case. The maximum repetition rate is limited within the PSU to stop the laser being externally triggered at an inappropriate repetition rate.

Laser Energy

This controls the amount of energy put into the flashlamp and hence will affect the output of the laser. The energy is adjusted by means of the q-switch delay.

Q-Switch Delay

This is the delay between triggering the flashlamp and triggering the q-switch. This value is set during laser test to provide the maximum output.



Figure 3.4 : Control Box

3.4.2 Calibration of PIV images

Calibration is used to spatially calibrate the camera images. The calibration is a map between camera pixels and world coordinates. The calibration is used in measurement to convert image displacement into world coordinates. Two-dimensional calibration is used to enter a calibration factor to compute the flow velocity using meters per second.

A calibration scale is placed in the plane of laser sheet. This calibration image is taken with camera and is processed in processing tab. Two points are selected on calibration scale which are

at known distance in mm and corresponding pixel displacement is found out. By using this logic, we get calibration factor in terms of mm/pixel.

$$\text{Velocity} = (\text{pixel displacement} * (\mu\text{m/pixel})) / \text{dt (in } \mu\text{secs)}$$

3.5 Thumb rules for PIV analysis

To get the best results from a PIV experiment, the image capture and the interrogation must match the flow. The parameters set to optimize the measurement are: the time between laser pulses (dT); image shifting; interrogation spot size; photograph magnification; light sheet dimensions; seed particle and seed concentration.

3.5.1 Interrogation spot size should be small enough for one vector to describe flow for that spot

This puts a limitation on the velocity gradient in an interrogation spot. If the velocity gradient is too large then the displacement peak becomes larger in area with a lower peak height, leading to the likelihood of measuring noise. Correlation produces the average velocity over the interrogation spot. The larger the spot, the more the averaging that takes place. To see the fine flow details, small spots are required. However, the minimum spot size is determined by Rule 2.

3.5.2 Spot should have more than ten particle image pairs per interrogation spot

The percentage of correct velocity measurements as a function of number of particle pairs has been established by Keane and Adrian. Their results are shown in Figure 3.5. These results show that the percentage of correct velocity measurements correlates strongly with the number of particle image pairs in the spot. As the concentration increases beyond one per spot, the percentage of valid measurements increases. This is because many pairs of particle images contribute to the displacement peak. The noise peaks caused by the correlation of the images of different particles decrease relative to the displacement peak. The loss of some pairs is tolerable because many others pairs are still creating the displacement peak.

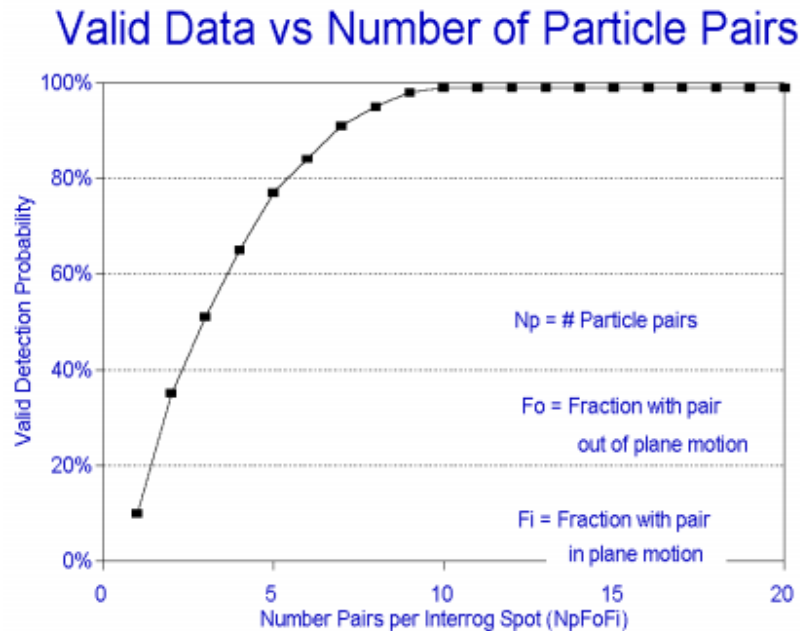


Figure 3.5 : Correlation of correct velocity measurements with the Number of particle images

Particle image concentrations with an average of one per interrogation spot produce the most erroneous measurements. This is because there is a high probability of having two pairs, or one and a half pairs or two half pairs in the interrogation spot. With two pairs of particles of equal size, the correlation for the distance between the two particles is as strong as the distance between the first and second image. With two pairs of particles of equal size, the wrong measurement is made fifty-percent of the time. With these low concentrations, a single particle that crosses the interrogation spot boundary can cause wrong measurements to be made.

The percentage of correct velocity measurements increases with decreasing particle image concentrations—from an average of one pair per spot down to very low concentrations. This is because where a pair of particles is found, it is unlikely that a second particle will also be in the spot to cause confusion about the correct pairing. A velocity measurement is only possible where a pair of particles is found so very low seeding concentration pictures produce sparse vector fields. If the goal of the experiment is to measure the flow on a high resolution grid, low seeding concentrations must be avoided. This increasing correct vectors with decreasing particle

concentrations assumes that the processor is set to reject areas with very low signals and that it can distinguish between the gray scale variations in background light and the particle images.

Effective seeding can be increased by increasing the interrogation spot size. With a larger interrogation spot there are more pairs per spot. When you increase the spot make sure that you are not violating the velocity gradient requirement of Rule 1. Decreasing the interrogation spot gives more velocity vectors with the same interrogation spot overlap. For high resolution work and for investigating small flow structures, you should select small interrogation spots.

3.5.3 Maximum in-plane displacements should be less than one-fourth interrogation spot size

This maximum displacement is a compromise between two parameters: Large displacements for the best percent of reading accuracy and small displacements to minimize lost pairs. As explained before, the velocity is measured by finding the location of the particle displacement peak. The location of the peak is measured with centroid or curve fit to a fraction of a pixel. The accuracy of the PIV measurement is a percent of full scale, or a number of pixels. The peak location error is the same wherever it is located, near the center zero velocity peak or near the edge. With large displacements the peak location error is a smaller percent of reading than small displacement peaks. The absolute maximum displacement that gives the correct displacement is half the interrogation spot. If large displacements are used, the FFT aliases, the peak location, and the measured peak give the wrong velocity. Lost pairs refers to particles that are inside the interrogation spot for only one laser pulse. In-plane motion causes particles to move across the spot border. Fast moving particles are more likely to lose a pair than the slow particles. Lost pairs creates a velocity bias towards slow velocity flow. The lost pair estimation is given in Rule 4. The compromise between these two objectives is $\frac{1}{4}$ spot displacement, to give good pairing and to use the accuracy of the system.

3.5.4 Maximum out-of-plane displacement should be less than one-fourth of light sheet thickness

This rule is established to keep the lost pairs (due to out-of-plane motion) to an acceptable level. In many experiments the light sheet is about 1 mm thick and the interrogation spot is 1 mm \times 1

mm. With this 1 mm cube measurement volume, the restrictions on out of-plane displacement is no greater than the in-plane displacement. With both in-plane and out-of-plane displacements considered, the estimated percentage of particles with pairs in the interrogation spot is:

$$\text{Percentage Paired} = (1-dX/X_{\text{spot}}) * (1-dY/Y_{\text{Spot}}) * (1-dZ/\text{Thick}) * 100\%$$

where

Percentage Paired = Percent of particles with a pair in the interrogation spot

dX = Particle image displacement in X direction

dY = Particle image displacement in Y direction

dZ = Particle image displacement in Z direction, out of plane motion

XSpot = Interrogation spot size in X direction

YSpot = Interrogation spot size in Y direction

Thick = Light sheet thickness

When the maximum one-fourth interrogation spot and light sheet thickness image displacement is used, an average of 42% of the particle images are paired. The seeding concentration must be increased for the lost pairs to get the same results. With one-fourth spot displacements in all three directions then the required seeding concentration is ten pairs per spot divided by the .42 paired, which is equal to 24 pairs per spot.

3.5.5 Minimum in-plane displacement should be two particle image diameters

If the particle image displacement is less than two particle image diameters, the image would be one elliptical particle image instead of two particle images. The autocorrelation zero peak and displacement peaks must be separated to accurately measure the centroid of the displacement peak. If the peaks overlap, the centroid will include some of the zero peak and bias the measurement towards zero displacement.

3.5.6 Exposure should be large enough to show particles

There are many factors that determine the exposure. These are:

- Laser energy
- Light sheet dimensions
- Camera Focal length number
- Photograph magnification
- Film Speed and resolution
- Particle size, and
- Particle material

Regarding particle scattering, particle size and material determine the scattered light power in the image of each particle. The particle scattering is in the Mie regime for most PIV applications. Mie scattering is complex and the scattered energy varies greatly with scattering direction, particle size, and particle index of refraction. The complexity of Mie scattering makes it difficult to make general statements about how much exposure is required for a given experiment. In most applications through trial and error, we find the correct exposure.

3.6 Interrogation and Cross-correlation of PIV images

Cross-correlation analysis is the act of correlating the first interrogation spot with a second spot which is offset in the mean flow direction. The purpose of this is to determine the distance that a particle has moved during the interrogation window; once the distance is known, the velocity can then be determined. This direct method quickly becomes cumbersome when large data sets are being analyzed. A much more efficient method is to estimate the cross-correlation functions by using Fast Fourier Transforms (FFT). FFTs work on the basic principle that adjacent interrogation spots are compared, thus reducing measurement noise and enhancing the displacement peak. Since only a single displacement peak is obtained with this method, it is ideal for flows that have reversals, since extra image shifting is unnecessary to resolve directional ambiguity.

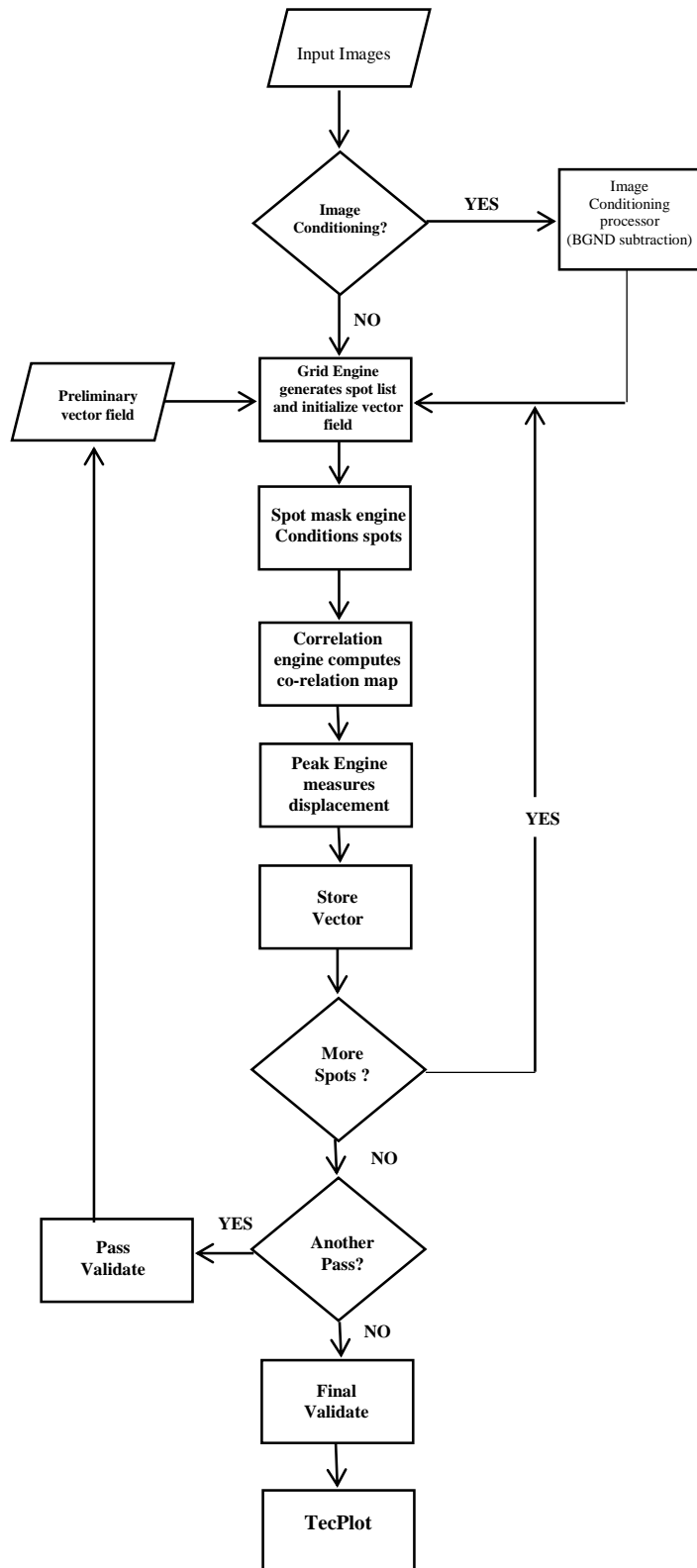


Figure 3.6 : PIV Processing Flowchart

3.6.1 Grid Engine

The Grid Engine breaks the input images up into smaller spots for processing and initializes the vector field. For each grid point, the process manager copies the pixels from the input images into the spots and passes the spots to the Spot Mask Engine.

Nyquist Grid

It is the classic PIV grid. It sets vectors with the x spacing equal to half Spot A width and the y spacing equal to half Spot A height. No spot offsets are used and the processing uses only a single pass. This gives a vector grid with 50% spot overlap fitting the Nyquist sampling criteria.

3.6.2 Spot Mask Engines

The Spot Mask Engine conditions the spots for processing and passes the spots to the Correlation Engine. It is used to modify or condition the image spots before processing. This can increase the signal-to-noise ratio of the correlation map.

Gaussian Mask

With Gaussian Mask, each pixel in spot A is multiplied by a Gaussian weighing function so that the spot is bright in the center and dark around the edges. This weighting gives more value to the center pixels and less to the edge pixels.

3.6.3 Correlation Engine

The Correlation Engine computes the correlation function and returns it as a correlation map. It computes the correlation function of the masked Spot A and Spot B returning the result as a correlation map. The correlation function is an algorithm that sums the particle image matches at all pixel displacements within the displacement range. The highest correlation map pixel is assumed to be the particle image displacement peak caused by the contributions of many particle pairs. Other peaks are assumed to be noise peaks caused by the random pairings of images of different particles.

FFT Correlation

It computes the correlation using Fast Fourier Transform (FFT). The spots must be square powers of 2 and the spot A must be the same size as the spot B. The Zero Pad Mask must be used when the two spots have different sizes.

3.6.4 Peak Engines

The Peak Engine finds the peak location in the correlation map.

Gaussian Peak

It locates the correlation peak with sub-pixel accuracy by fitting a Gaussian curve to the highest pixel and its four nearest neighbors. Two 3-point fits are done: one in the x direction with the peak pixel and the pixels to the left and right of the peak; and one in the y direction with the peak pixel and the pixels above and below the peak.

3.7 Experimental Procedure

Figure 3.7 shows the RTS test setup as explained in chapter 3 consisting of rectangular tank which is executing reciprocating motion with given excitation frequency. For PIV study, laser is fired from the top of the tank and laser sheet falls at center of the tank. Seeding particles are added in the flow which are illuminated by laser light and follows the flow to give velocity contours in the flow field. To capture the flow camera is placed perpendicular to laser sheet.

With synchronizing the laser pulse and camera, two serial images with short time interval were captured. Images are captured at different crank angles and repeatability test is performed to check correctness of experiment. Using the two serial images, the two-dimensional velocity distributions were calculated using the cross-correlation technique. An image averaging is done over 10 images to get averaged image at a particular crank angle and velocity contours are plotted for this image. Experiment is performed for 40% fill in linear and weakly nonlinear sloshing regime at 90°, 135°, 225° and 270°.



Figure 3.7: PIV Experimental setup

Chapter 4

Numerical Model

4.1 Numerical Modelling:

Sloshing is characterized by strong nonlinear fluid motion where it is difficult to solve the governing equations analytically. Also analytical solutions can be used only for linear sloshing regime with small amplitudes. Sloshing noise depends on the tank geometry and to reduce this noise certain modifications are required in tank geometry by introducing baffles which is expensive by performing experiments. For such iterative process, experiments are laborious, time consuming and costly as it involves sensors and data acquisition system. This necessitates the importance of numerical modelling.

The time accurate multiphase CFD modelling was used to capture the sloshing phenomenon when the tank was subjected to a controlled excitation. The numerical method used in the present work is a finite volume method that solves the integral form governing equations. In this method the governing differential equations are integrated over a control volume enclosed by a control surface. The governing equations in fluid flow are conservation of mass and momentum. For modeling free surface flow in tank volume of fluid (VOF) method is used. Transport equation together with conservation of mass and momentum are employed to follow the free surface changes. Commercial CFD software Star CCM+ v9.06 was used in this study. Figure 4.1 shows the CFD simulation procedure.

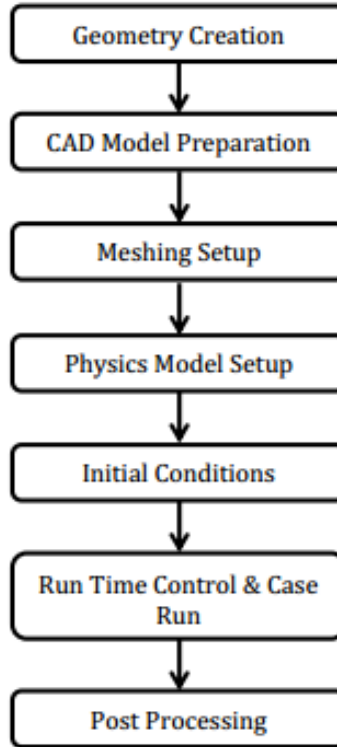


Figure 4.1: CFD Simulation Procedure

4.1.1 Geometry Creation:

A 3D geometry of tank (0.238*0.22*0.238 m) is prepared in Star CCM+ which is having same dimensions as in case of experiment. The meshing cannot be used for geometry parts or body. In order to mesh geometry parts, they must be assigned to one or more regions, and the mesh is then generated for the region. Each part surface is assigned to boundary and each part curve is assigned to feature curve. In this way, front , back, left, right, top and bottom boundary is created and wall boundary condition is used for each wall.

4.1.2 Meshing Setup:

A mesh is the discretized representation of the computational domain, which the physics solvers use to provide a numerical solution. It can be classified based on elements and connectivity of cells.

Based on elements:

Meshes can also be classified based upon the dimension and type of elements present. Depending upon the analysis type and solver requirements, meshes generated could be 2-dimensional (2D) or 3-dimensional (3D). Common elements in 2D are triangles or rectangles, and common elements in 3D are tetrahedral or bricks.

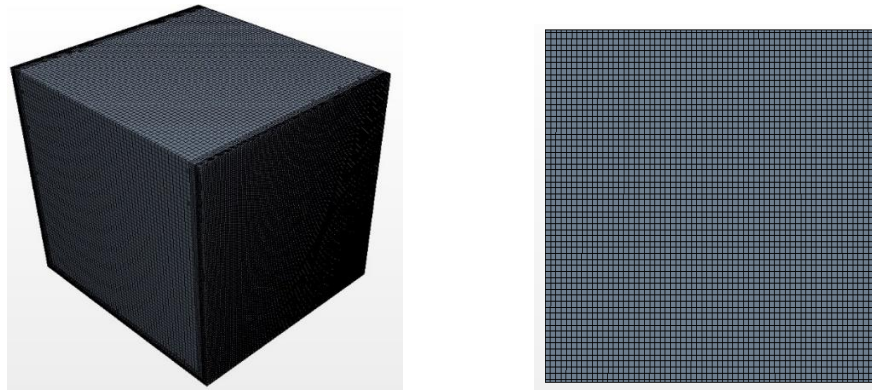


Figure 4.2 : 3D and 2D computational Grid

Based on connectivity:

The most basic form of mesh classification is based upon the connectivity of the mesh: structured or unstructured Mesh.

Structured Meshes

A structured mesh is characterized by regular connectivity that can be expressed as a two or three dimensional array. This restricts the element choices to quadrilaterals in 2D or hexahedra in 3D. The regularity of the connectivity allows us to conserve space since neighborhood relationships are defined by the storage arrangement.

Unstructured Meshes

An unstructured mesh is characterized by irregular connectivity is not readily expressed as a two or three dimensional array in computer memory. This allows for any possible element that a solver might be able to use. Compared to structured meshes, the storage requirements for an

unstructured mesh can be substantially larger since the neighborhood connectivity must be explicitly stored.

A mesh is composed of the following mesh entities:

- **Vertex** - A vertex is a point in space that you can define with a position vector. A number of vertices can be used to define a feature curve or a face.
- **Face** - A face comprises an ordered collection of vertices such that they define a surface in three-dimensional space.
- **Cell** - A cell is an ordered collection of faces that defines a closed volume in space.

Meshing options used for the simulation methodology are as follows:

- ❖ **Prism layer Mesher** - Prism layer Mesher is used with a core volume mesh to generate orthogonal prismatic cells next to wall surface or boundaries which makes the solution more accurate near the wall surface. A prism layer is defined in terms of its thickness, the number of cell layers within it, the size distribution and function of distribution for these layers.
- ❖ **Surface Remesher** - Surface Remesher is used to retriangulate the existing surface and hence optimize it for the volume mesh models. The remeshing is based on a target edge length and can refine the mesh based on curvature and surface proximity. It improves the sub surface meshing when prism layer meshing is used.
- ❖ **Trimmer** - Trimmer mesh is used for producing high quality grids with minimal cell skewness and the refinement done is based upon the surface mesh size and other control factors. The trimmer meshing model utilizes a template mesh that is constructed from hexahedral cells from which it cuts or trims the core mesh using the starting input surface.

Following are the user defined controls that were taken under consideration while meshing the considered geometry:

- ❖ **Base Size:** The base size is a reference length used in other meshing parameters. It can be set either as a relative value or as an absolute value. Mesh independence study was done and it was found that 64*64*64 mesh is used for CFD analysis and base Size=3.671875 mm is taken for geometry under consideration.
- ❖ **Maximum Cell Size:** The maximum cell size limits the largest cell size so that mesh is not too coarse in the center of the domain. It can be set either as a relative value or as an absolute value. It was defined relative to the base size and the value was kept as 100%.
- ❖ **Prism Layer Thickness:** It specifies the total thickness of the prismatic cell layers. It can be set either as a relative value or as an absolute value. It was defined relative to the base size and the value was kept as 10%.
- ❖ **Surface Size:** Surface Size is adopted as minimum and maximum and the size is taken as 100% relative to the base size, both for minimum and maximum.

4.2 Numerical Formulation:

The Navier Stokes equations are solved by using Segregated or uncoupled Flow algorithm. The linkage between the momentum and continuity equations is achieved with a predictor corrector approach. The method used to solve these equation is based on collocated variable arrangement and Pressure velocity coupling is taken care by Rhie-Chow Interpolation combined with a SIMPLE type Algorithm. The whole flow field is initialized by some velocity and pressure field thus calculating initial mass fluxes.

The flow equations are solved providing an intermediate velocity field and mass fluxes at faces. This intermediate velocity field and fluxes are utilized to solve pressure correction equation and hence giving pressure field as output. The flow equations are again solved using this updated pressure field along with intermediate velocity field. This loop continued till we get a converged pressure field corresponding to predicted velocity field. When both momentum equation and pressure field are converged the solution migrates to next time step.

Equations involved are

Momentum Equation:

$$\frac{\partial}{\partial t} \int_V (\rho v dV) + \int_S (\rho v \cdot dS) = - \int_S \rho I \cdot dS + \int_S T \cdot dS + \int_V \rho b dV \quad (1)$$

Continuity Equation:

$$\frac{\partial}{\partial t} \int_V (\rho dV) + \int_S (\rho v \cdot dS) = 0 \quad (2)$$

Where ρ stands for fluid density, v stands for fluid velocity vector. Control volume surface under consideration is defined by area S and volume V , T stands for stress tensor, p is the pressure term and I is the kronecker delta function, and b is the body forces vector per unit mass.

Due to high Reynolds number the flow is turbulent. The comparison is done in chapter 5 between different turbulence models and $k-\varepsilon$ turbulence model is chosen for further analysis. The Realizable two layer $k-\varepsilon$ model is used for turbulence modelling. The $k-\varepsilon$ turbulence model is a two –equation model in which transport equations are solved for turbulent kinetic energy k and its dissipation rate ε . Realizable $k-\varepsilon$ uses a modified equation for turbulent dissipation rate ε . A critical coefficient of the model C_μ is expressed as a function of mean flow and turbulence properties. This variable C_μ is consistent with experimental observations in boundary layer. This model combines the Realizable $k-\varepsilon$ model with the two layer approach.

The two layer approach allows the $k-\varepsilon$ model to be applied in viscous sublayer. In this approach, the computation is divided into two layers. In the layer next to the wall, the turbulent dissipation rate ε and the turbulent viscosity μ_t , are specified as functions of wall distance. The value of ε specified in the near-wall layer are blended smoothly with the values computed from solving the transport equations far from the wall.

General equation used for modelling k and ϵ :

$$\frac{d}{dt} \int_V (\rho \Phi dV) + \int_S (\rho \Phi (v - v_g) \cdot dS) = - \int_S \Gamma \nabla \Phi \cdot dS + \int_V \rho b \Phi dV \quad (3)$$

Where ρ stands for fluid density, v stands for fluid velocity vector. Control volume surface under consideration is defined by area S and volume V , T stands for stress tensor, p is the pressure p and I is the kronecker delta function, Φ defines scalar variable (k or ϵ), Γ denotes the diffusivity coefficient, b is the body forces vector per unit mass and $b\phi$ represents sources or sinks of ϕ .

The Volume of fluid method is utilized for tracking and locating the free surface motion during sloshing in tank. The VOF method adopts volume fraction as the variable for spatial distribution of each phase at a given time instant. Volume Fraction of a phase can be defined in terms of the ratio of the volume occupied by the phase to the computational cell volume.

The VOF model assumes that velocity, pressure, and temperature fields are shared by all immiscible fluid phases present in a control volume. The equations describing mass, momentum and energy transport are solved in the same way as solved for single phase flow but for an equivalent fluid whose physical properties are calculated as functions of the physical properties of its constituent phase and their respective volume fractions at that time instant.

$$\rho = \sum_i \rho_i \alpha_i \quad (4)$$

$$\mu = \sum_i \mu_i \alpha_i \quad (5)$$

Where $\alpha_i = \frac{V_i}{V}$ the volume fraction and ρ_i and μ_i is the density and molecular viscosity of the i^{th} phase. The sum value of volume of fraction is one at any point in the flow domain.

$\sum_{i=1}^n \alpha_i = 1$, Where n is number of phases present in the flow domain. The interface is tracked by solving a transport equation for the volume fraction of phases.

For the i^{th} phase, it is expressed as:

$$\frac{\partial}{\partial t} \int_V (\alpha_i dV) + \int_S (\alpha_i v \cdot dS) = 0 \quad (6)$$

An immiscible phase mixture of water and air is assumed in Sloshing Phenomenon. Since it is an immiscible phase mixture, hence the fluid components are always separated by a sharp interface. The High-Resolution Interface Capturing (HRIC) scheme is used for tracking sharp interfaces. The scheme is based on utilization of a normalized variable $\{\xi\}$.

The normalized variable for center cell is defined as

$$\xi_c = \frac{\alpha_D - \alpha_u}{\alpha_D - \alpha_u} \quad (7)$$

The normalized face value ξ_f is defined as

$$\xi_c = \begin{cases} \xi_c & \text{if } \xi_c < 0 \\ 2 \xi_c & \text{if } 0 \leq \xi_c \leq 0.5 \\ 1 & \text{if } 0.5 \leq \xi_c \leq 1 \\ \xi_c & \text{if } 1 \leq \xi_c \end{cases} \quad (8)$$

The final correction of ξ_f is based on angle θ between normal to interface n_i and the cell face surface vector a_f as given by:

$$\xi'_f = \xi_f (\cos \theta)^{C_\theta} + \xi_c (1 - (\cos \theta)^{C_\theta}) \quad (9)$$

The cell face value α_f is calculated as

$$\alpha_f = \xi'_f (\alpha_D - \alpha_u) + \alpha_u \quad (10)$$

The solution of Navier-Stokes equations follows the segregated iterative method, in which the linearized momentum component equations are solved first using prevailing pressure and mass fluxes through cell faces (inner iterations), followed by solving the pressure-correction equation derived from the continuity equation. SIMPLE Algorithm is used to solve the Navier-Stokes equation and converged velocity field is achieved for each time step. After getting corrected velocity field from momentum equation, equations for volume fraction and k-epsilon model are solved. The whole process moves to next time step when residual of all the equations included in this process is reduced to a defined level.

Boundary Condition for all the faces of tank is described as no-slip wall. No slip wall means that the tangential velocity is set either to zero or to a specified value. In our test case the value is assigned as zero. The boundary face pressure is extrapolated from the adjacent cell using reconstruction gradients. As the computational domain fully enclosed, a location for reference pressure is defined at center of top wall of tank.

The Simple Algorithm used in numerical study is discussed in flow chart given in Figure 4.3.

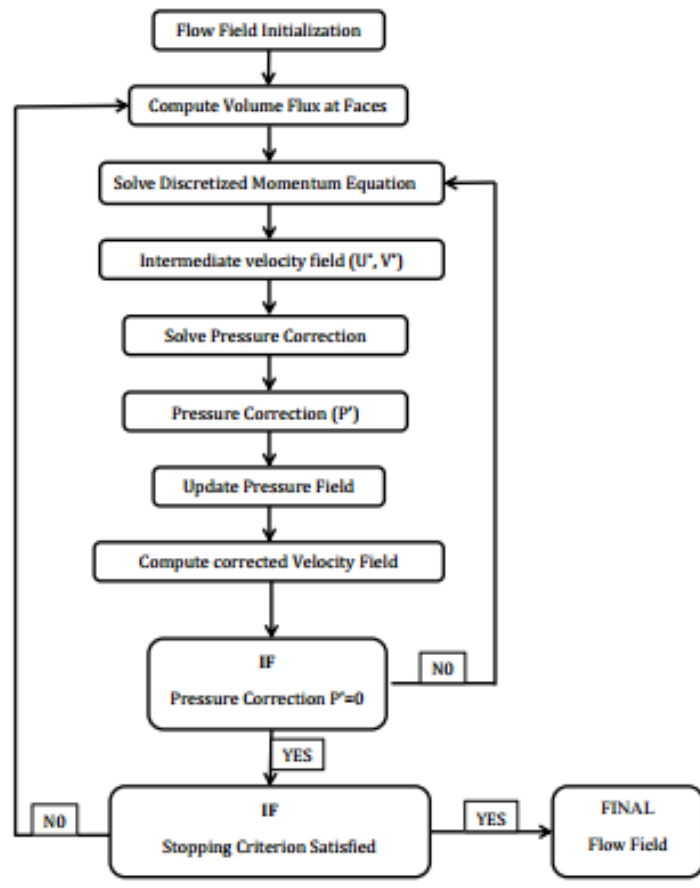


Figure 4.3 : SIMPLE Algorithm

Chapter 5

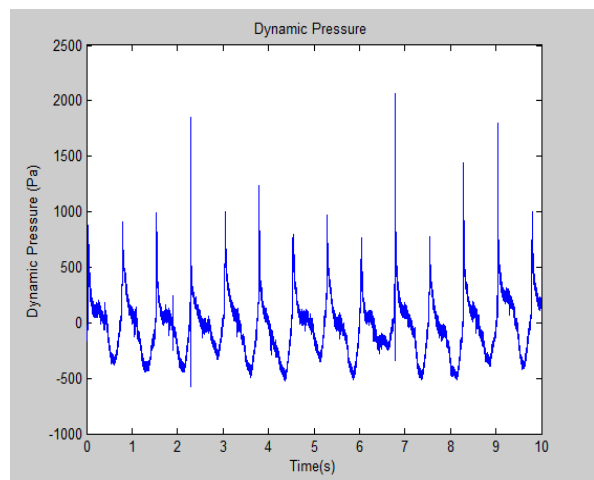
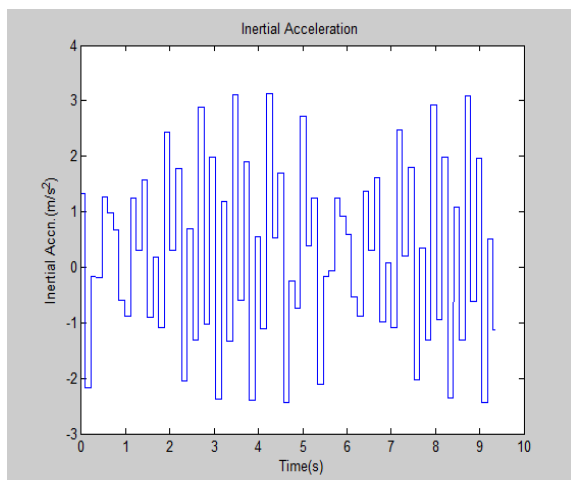
Results and Discussion

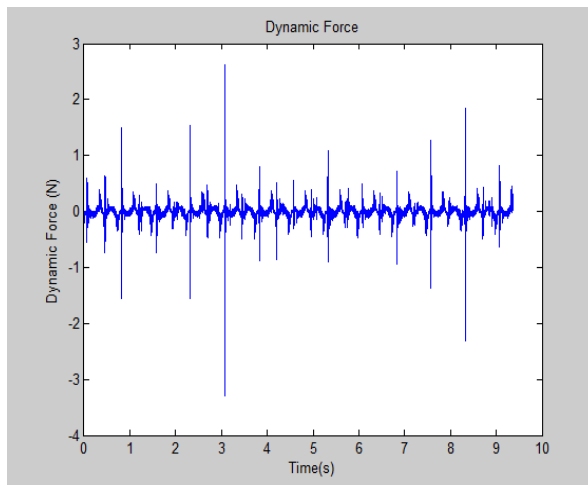
5.1 Experimental Results

In this section, experimental results are presented for various parametric studies. The sensors were placed at a height of 10 % of tank height and 10 % below the liquid surface. It is observed from the inertia acceleration sensor data that acceleration in downward direction (Z direction) is 1 g and is constant with time. Lateral acceleration (Y) is less than 0.1 g and therefore indicating negligible lateral movement. A line sensor placed on the vehicle triggers the data acquisition system as the sensor recognizes the change in Infra-red reflectivity of light (from Black to White) from the track below it. The Figures show the recorded test data of inertia acceleration in longitudinal direction, dynamic pressure and dynamic force on tank walls.

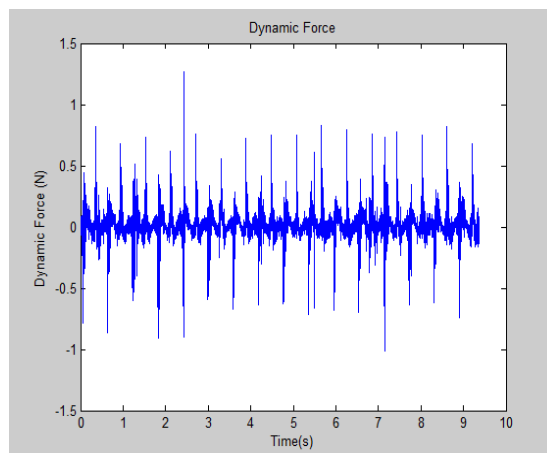
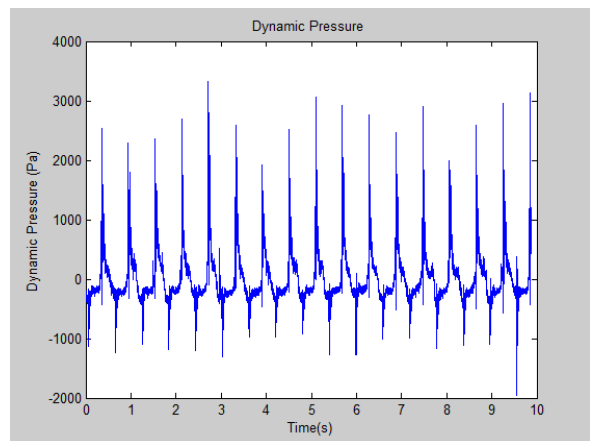
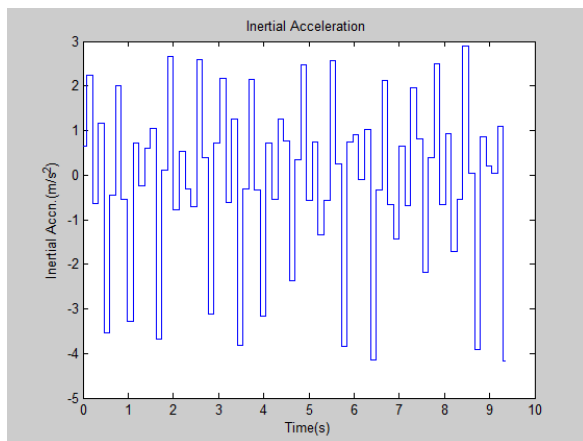
5.1.1 Variation in fill level keeping excitation frequency constant

Experiments are conducted for 20%, 40% and 60% fill for nonlinear sloshing regime. Figure A,B,C shows the inertial acceleration of tank , dynamic pressure and dynamic force on tank walls. Sensors are located at a height of 10 % of tank height and 10 % below the liquid surface.

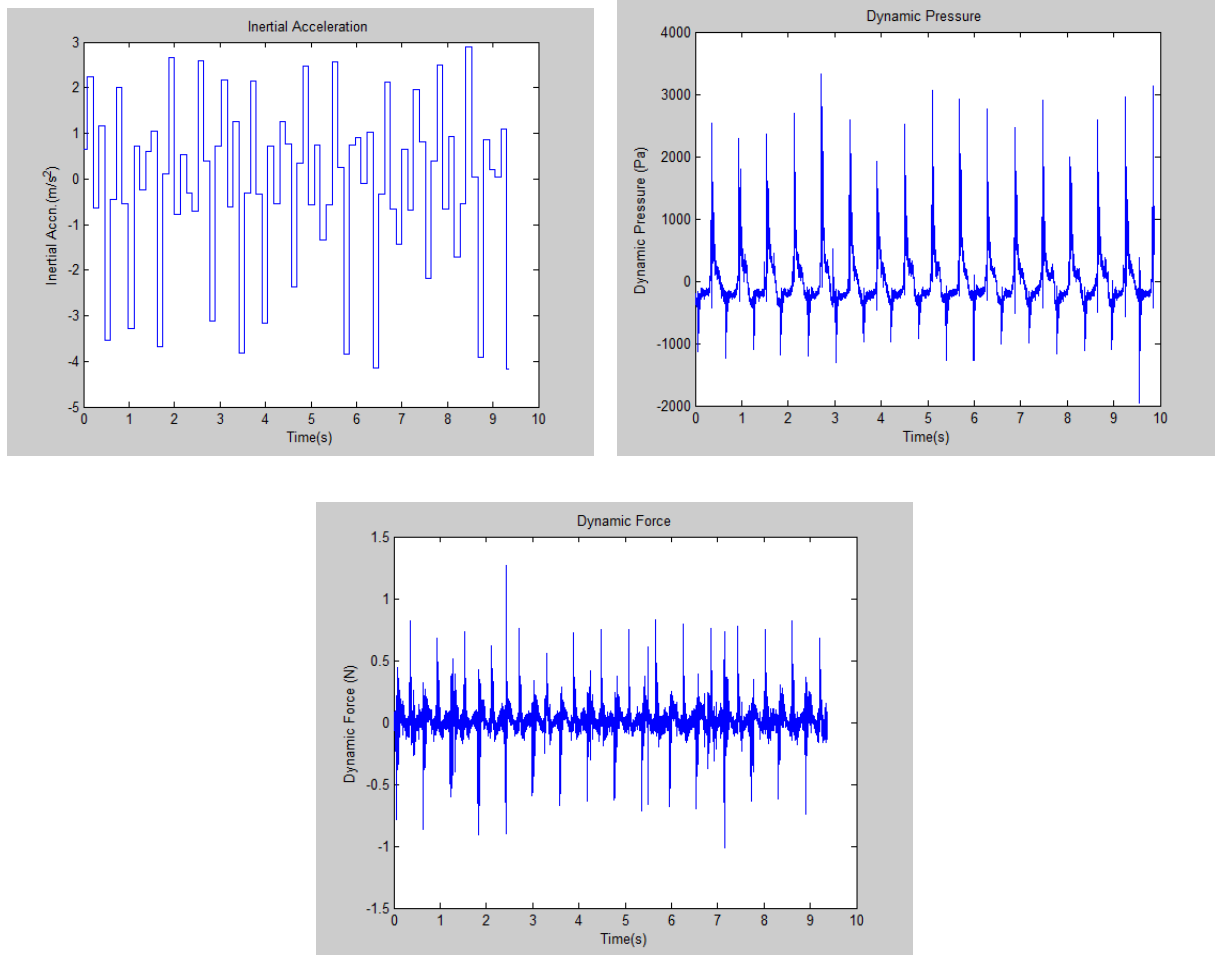




A: Experimental data for 20% fill for nonlinear sloshing



B: Experimental data for 40% fill for nonlinear sloshing

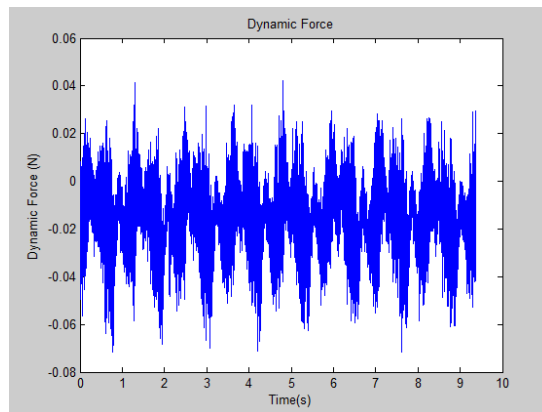
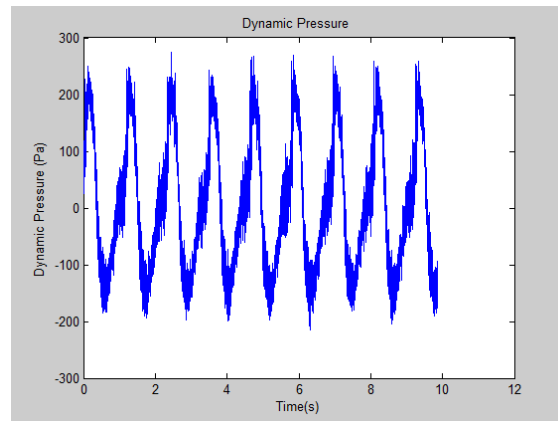
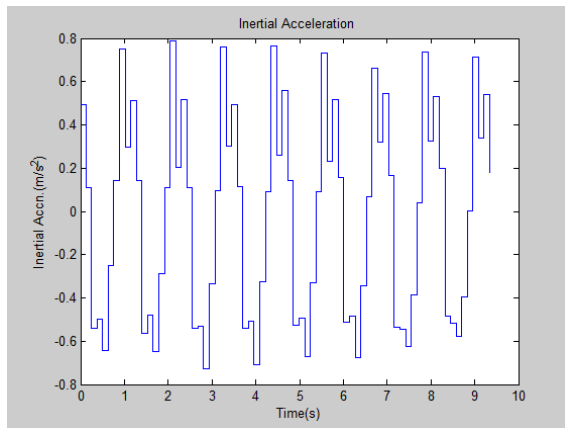


C: Experimental data for 60% fill for nonlinear sloshing

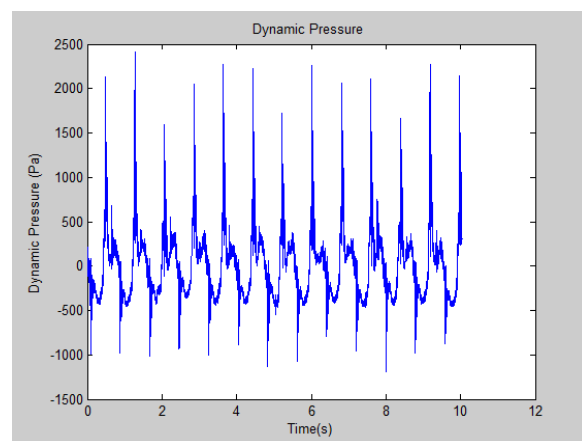
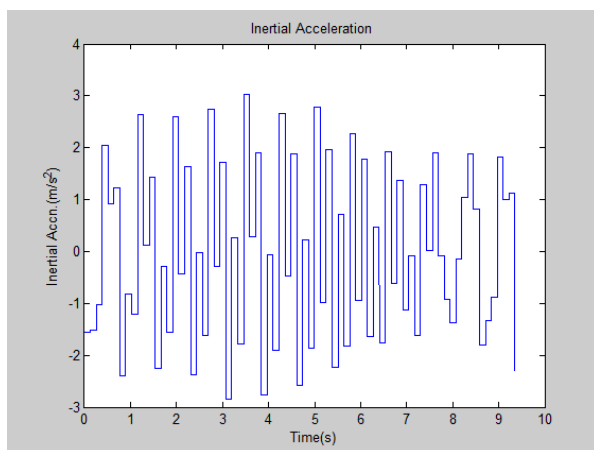
Figure 5.1.1: Experimental inertial acceleration, dynamic pressure and dynamic force data for 20%, 40% and 60% fill for nonlinear sloshing

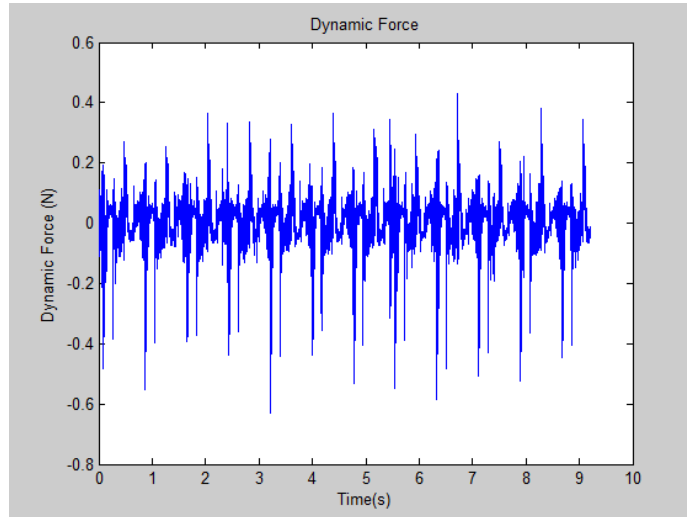
Events are occurring at the same time as seen from inertial acceleration, dynamic pressure and dynamic force plot. So data is synchronous. Cycle to cycle variation is seen in plots due to nonlinearity of fluid motion inside the tank.

5.1.2 Variation in excitation frequency keeping for 40% fill level

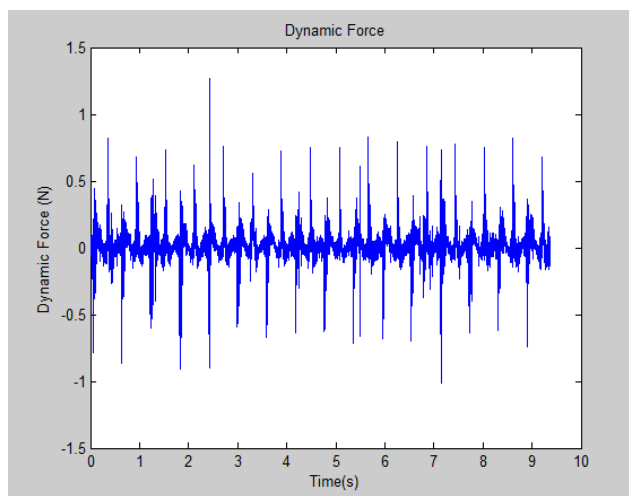
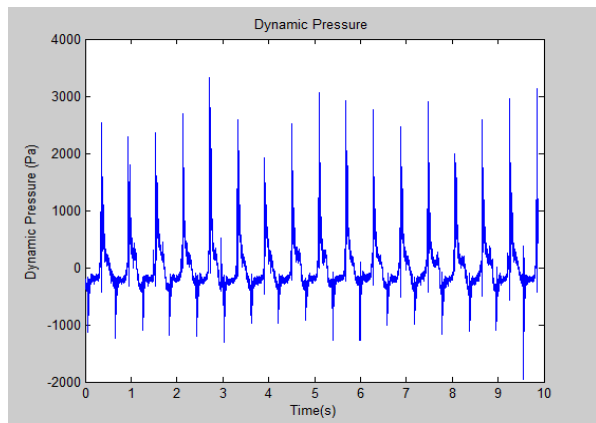
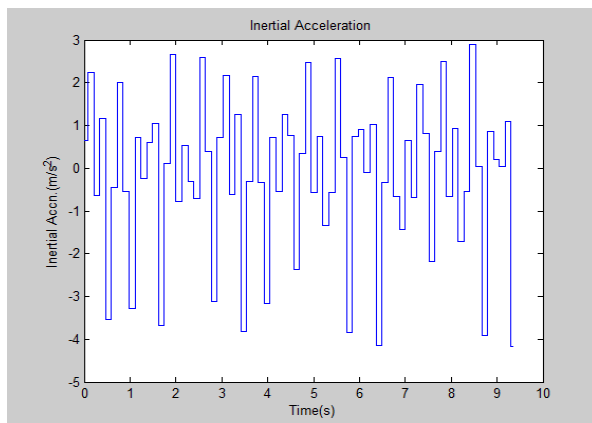


A: Experimental data for 40% fill and 0.5fs for linear sloshing





B: Experimental data for 40% fill and 0.75fs for nonlinear sloshing



C: Experimental data for 40% fill and 1fs for nonlinear sloshing

Figure 5.1.2: Experimental inertial acceleration, dynamic pressure and dynamic force data for 40% fill for excitation frequency of 0.5fs, 0.75fs and 1fs

Events are occurring at the same time as seen from inertial acceleration, dynamic pressure and dynamic force plot. So data is synchronous. Cycle to cycle variation is seen in plots due to nonlinearity of fluid motion inside the tank. As we move from linear sloshing regime to nonlinear sloshing regime, dynamic pressure and dynamic force increases.

5.2 CFD Analysis

5.2.1 Mesh independence study

Mesh independence study was done for mesh size of 32*32*32, 64*64*64 and 128*128*128 for 20% fill, excitation frequency =0.75 fs and pressure probe location at 10% of tank height. The dynamic pressure plot for back boundary is shown in Figure 5.2.1.

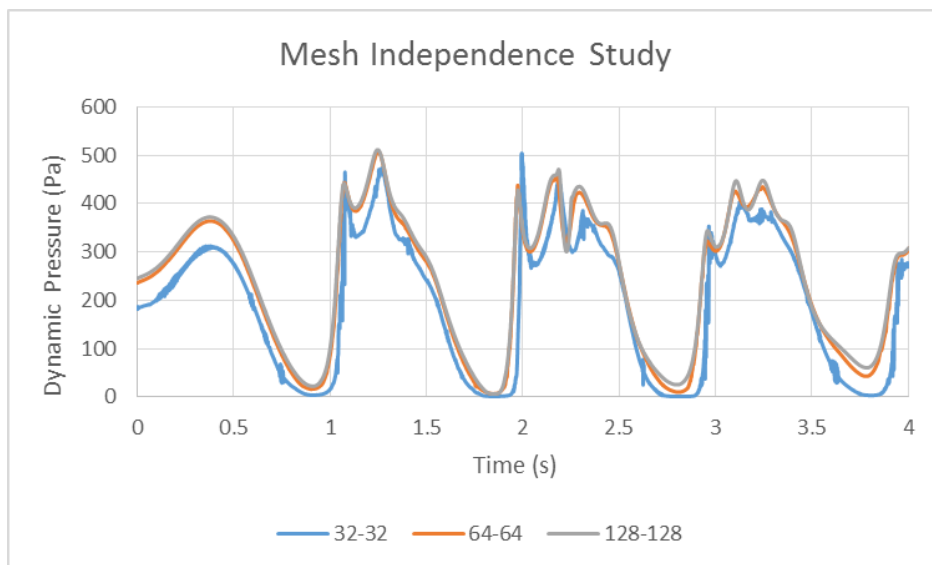


Figure 5.2.1: Mesh Independence Study

It can be seen from plots shown in Figure 5.2.1 that the three plots follow similar trend and do not show any significant difference in terms of magnitude. However the difference between 64*64*64 and 128*128*128 is not significant. Therefore, for future study a mesh size of 64*64 can be used.

5.2.2 Effect of turbulence

For 20% fill level and excitation frequency of 0.75fs, study of effect of turbulence on sloshing phenomenon is done. The aim of this study was to predict the difference between turbulent models. The turbulence models that were taken under consideration were Spalart Allmaras Model, K-Epsilon Model and k-omega model. The inviscid flow is an idealized situation in which viscous effects are neglected and governing equations are obtained by discarding the viscous term in Navier Stoke's equation and solving these equations would not resolve boundary layer and other viscous effects arising in the flow. Viscous flows which take viscosity under consideration and can be divided into laminar and turbulent flow and are differentiated on the basis of Reynold's Number. Turbulent flows are the flows that include continuous instability, exhibit irregular, small-scale, highly fluctuating flows in both space and time. There are a number of models that can simulate these flows but every model is accompanied with certain limitations. The Spalart Allmaras Model solves an equation for turbulent viscosity (ν_t) in terms of $\tilde{\nu}$ where $\tilde{\nu}$ is related to ν_t as $\nu_t = \tilde{\nu} f_v$. The k- ϵ model solves two equations for k and ϵ which in turn defines the value of turbulent viscosity (ν_t). Similarly k- ω model solves two equations for k and ω which in turn defines the value of turbulent viscosity (ν_t). This value of turbulent viscosity is used in solving RANS equation.

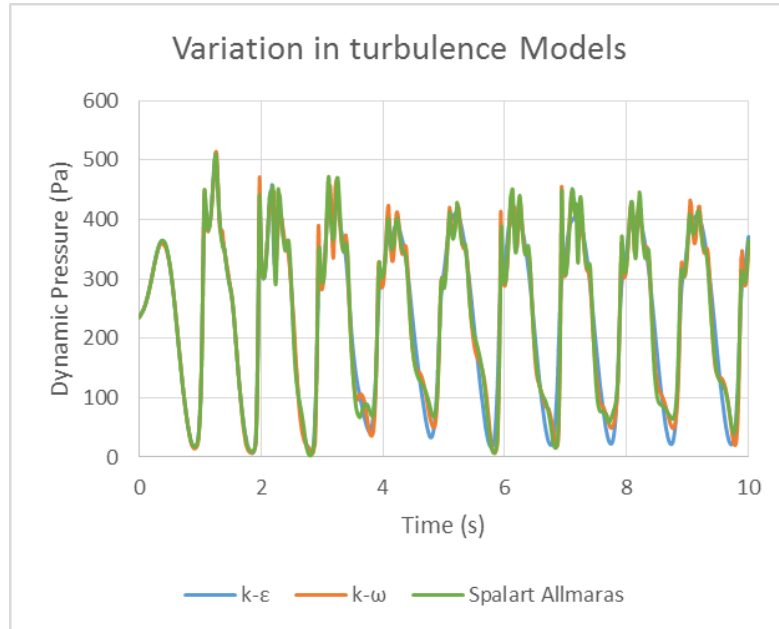


Figure 5.2.2: Effect of turbulence models

Results obtained for all the other three models are quite similar as seen from figure 5.2.2. As k-ε turbulence model is a more complete model, it was used for all the simulations in this study. The first variable, k, determines the turbulence kinetic energy whereas the second variable, ε, the dissipation rate of the turbulence kinetic energy. Together they give an estimate of the length and time scale in the turbulent flow.

5.3 Wave Height Comparison

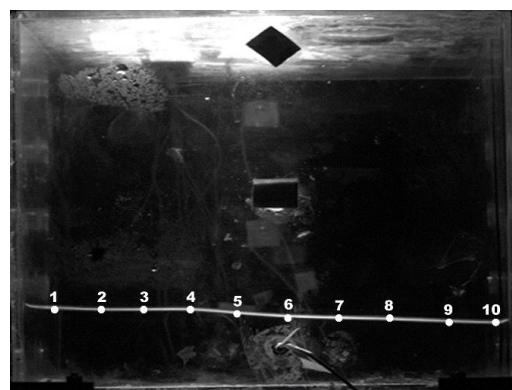
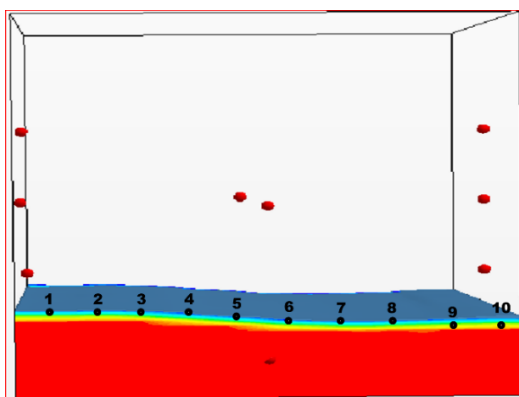
In order to validate the CFD model, VOF wave height captured for simulation were compared with high speed camera images recorded during experimentation. The CFD simulation were carried out using inertial acceleration data recorded during the experimental study. This study has been carried out for two fill levels of 20 % and 40 % in linear and weakly nonlinear sloshing regime. To quantify the comparison between the CFD and experimental results, the difference between the liquid surface height obtained from CFD and experiment is compared and tabulated in tables attached besides the comparison. Several points were defined on the liquid surface and the ratio of interface height to distance from front wall is tabulated. This comparison is

performed in the near linear sloshing regime because in the non-linear sloshing regime, there is large entrapment of bubbles which make the image interrogation for liquid surface very difficult. It must also be noted that the image interrogation technique presented here has a few sources of uncertainty which are:

1. Liquid surface determination for bubbly flow is difficult to measure
2. Liquid surface height is again difficult measure when the liquid height is small because meniscus effect due to wall wetting leads to uncertainty of surface location.
3. Perspective projection of a 3D image on a 2D surface leads to parallax effects which may again lead to uncertainty in image interrogation.

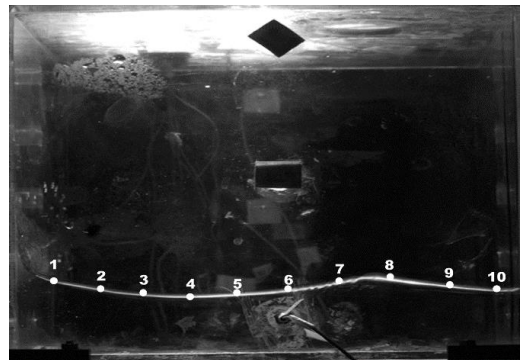
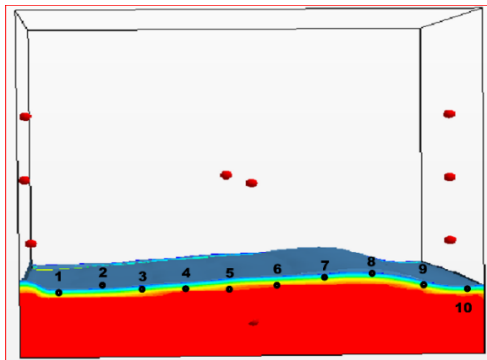
These uncertainties are higher in non-linear flow regime and subsequently decrease in the linear slosh regime. Hence the measurements presented are in the linear and weakly nonlinear sloshing regime.

5.3.1 Wave height analysis for 20% fill in linear and weakly nonlinear sloshing



Point	CFD	EXPT	CFD - EXPT
1	0.0512	0.048	0.0032
2	0.048	0.0485	-0.0005
3	0.0494	0.0485	0.0009
4	0.0468	0.0451	0.0017
5	0.0442	0.0438	0.0004
6	0.0427	0.0422	0.0005
7	0.0424	0.0432	-0.0008
8	0.0434	0.0404	0.003
9	0.0431	0.0414	0.0017
10	0.0442	0.04	0.0042

Figure 5.3.1.1: Wave height comparison for 20% fill and 0.5fs in linear sloshing regime



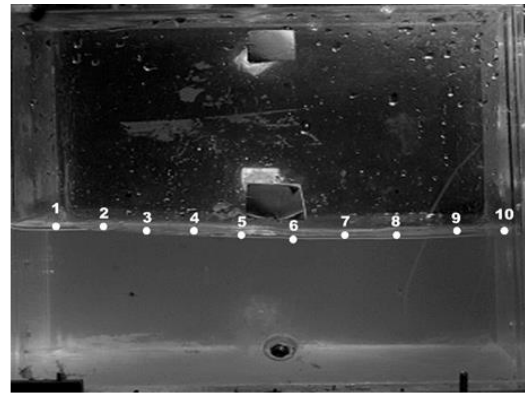
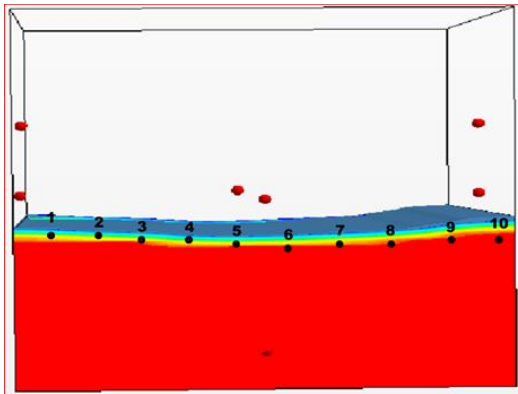
Point	CFD	EXPT	CFD - EXPT
1	0.0428	0.046	-0.0032
2	0.0437	0.0405	0.0032
3	0.0465	0.038	0.0085
4	0.0491	0.038	0.0111
5	0.05	0.0405	0.0095
6	0.0522	0.043	0.0092
7	0.0522	0.0504	0.0018
8	0.05	0.0475	0.0025
9	0.045	0.043	0.002
10	0.043	0.042	0.001

Figure 5.3.1.2: Wave height comparison for 20% fill and 0.75fs in nonlinear sloshing regime

From figure 5.3.1.1, it is clearly seen that the interface in CFD in HS video matches well in linear sloshing regime. From table it can be seen that the maximum difference between CFD and experiment is 0.0042 m. In CFD , cell size used is 0.0037 m and interface thickness is of two-three times the cell size. So CFD compares well with experiment in linear sloshing regime.

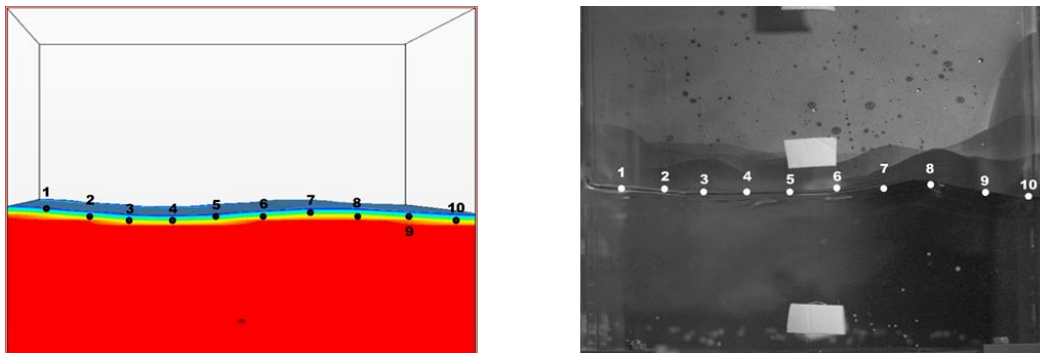
Similarly, from figure 5.3.1.2, it is seen that there is discrepancy in measuring interface height in CFD and HS video where peaks and troughs are seen in nonlinear sloshing regime. From table it can be seen that the maximum difference between CFD and experiment is 0.0095 m which is well within the uncertainty in CFD wave height measurement.

5.3.2 Wave height analysis for 40% fill in linear and weakly nonlinear sloshing



Point	CFD	EXPT	CFD - EXPT
1	0.097	0.1	-0.003
2	0.0956	0.0978	-0.0022
3	0.094	0.0963	-0.0023
4	0.0917	0.0947	-0.003
5	0.0928	0.0925	0.0003
6	0.0934	0.093	0.0004
7	0.0955	0.0943	0.0012
8	0.0977	0.095	0.0027
9	0.1	0.0978	0.0022
10	0.1	0.0979	0.0021

Figure 5.3.2.1: Wave height comparison for 40% fill and 0.5fs in linear sloshing regime



Point	CFD	EXPT	CFD - EXPT
1	0.105	0.11	-0.005
2	0.093	0.1	-0.007
3	0.0946	0.108	-0.0134
4	0.0945	0.108	-0.0135
5	0.0955	0.107	-0.0115
6	0.0983	0.112	-0.0137
7	0.0982	0.12	-0.0218
8	0.0957	0.112	-0.0163
9	0.0954	0.102	-0.0066
10	0.094	0.106	-0.012

Figure 5.3.2.2: Wave height comparison for 40% fill and 0.6fs in weakly nonlinear sloshing regime

From figure 5.3.2.1, it is clearly seen that the interface in CFD in HS video matches well in linear sloshing regime. From table it can be seen that the maximum difference between CFD and experiment is 0.003 m. In CFD , cell size used is 0.0037 m and interface thickness is of two-three times the cell size. So CFD compares well with experiment in linear sloshing regime.

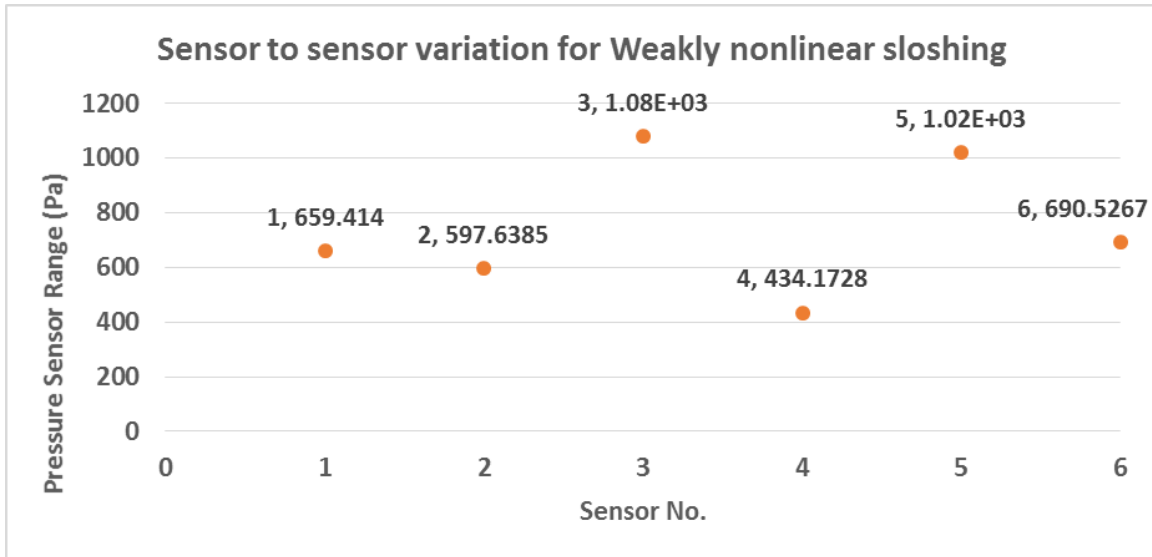
Similarly, from figure 5.3.2.2, it is seen that there is discrepancy in measuring interface height in CFD and HS video where peaks and troughs are seen in nonlinear sloshing regime. From table it can be seen that the maximum difference between CFD and experiment is 0.0218 m which is approximately two times the uncertainty in CFD wave height measurement.

5.4 Dynamic Pressure comparison between CFD and experiment

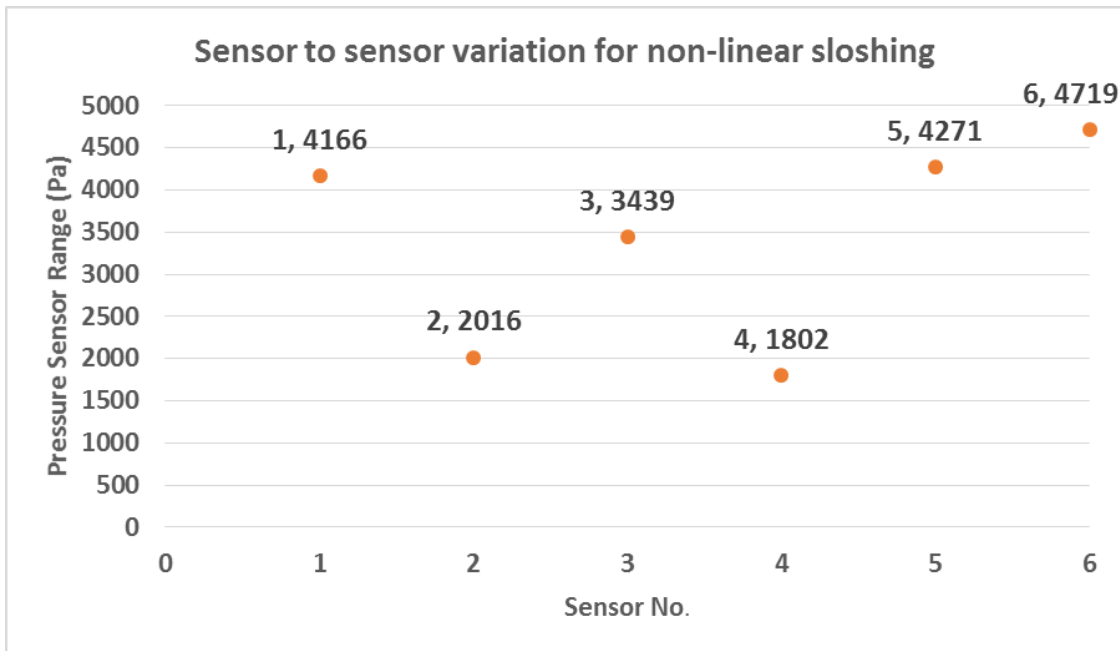
The dynamic pressure sensor used in the experiments consist of quartz discs attached to a diaphragm. Pressure acting on the diaphragm compresses the quartz discs and produce electrical charge which is converted to pressure acting on the sensor using sensitivity of the respective sensor. The Pressure obtained from CFD is the pressure field obtained when all the equations of CFD model are converged.

5.4.1 Uncertainty in experimental pressure measurements

To calculate the uncertainty in the experimental pressure measurements, pressure sensor uncertainty test is carried out for 20% fill level. Different pressure sensors are located at a location of 10 percent below fill level to see the sensor to sensor variation. Pressure range is defined as the difference between maximum pressure and minimum pressure for a given cycle and average of all these pressure range over a cycle is calculated. Figure 5.4.1 shows the uncertainty in experimental pressure measurements including sensor to sensor variation in weakly nonlinear and nonlinear sloshing regimes.



A: Sensor to sensor variation for weakly nonlinear sloshing



B: Sensor to sensor variation for nonlinear sloshing

Figure 5.4.1: Uncertainty in experimental pressure measurements

If we discard sensor 2 and 4,

In figure 5.4.1 A, in weakly nonlinear regime,

Maximum value of pressure range = 1080 Pa

Minimum value of pressure range = 659.414 Pa

Uncertainty = 420.586 Pa

Uncertainty in the experimental pressure measurements in weakly nonlinear regime is 420.586Pa.

In figure 5.4.1 B, in nonlinear regime,

Maximum value of pressure range = 4719 Pa

Minimum value of pressure range = 3439 Pa

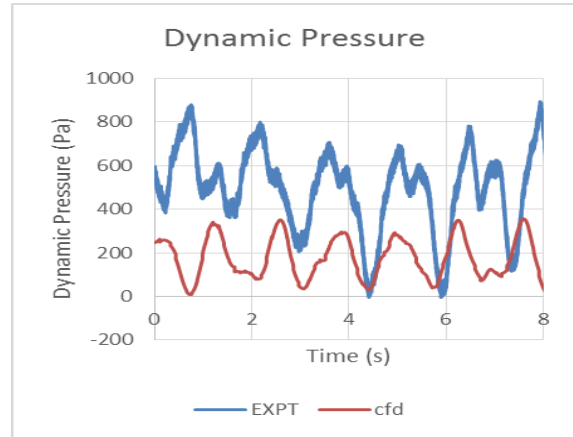
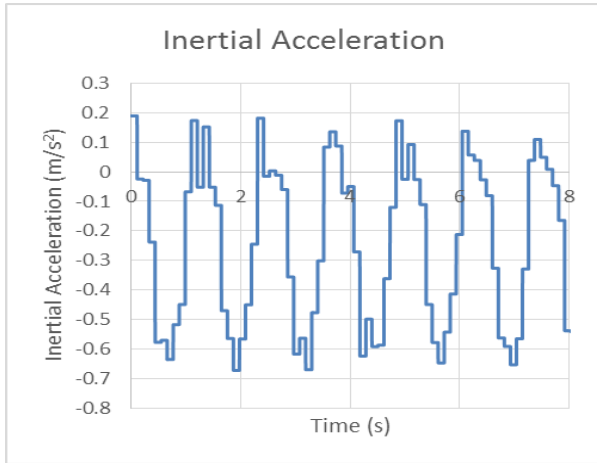
Uncertainty = 1280 Pa

Uncertainty in the experimental pressure measurements in nonlinear regime is 1280 Pa.

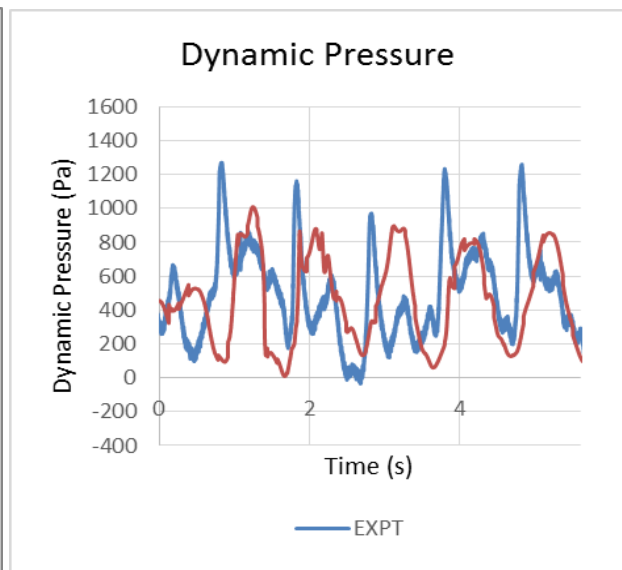
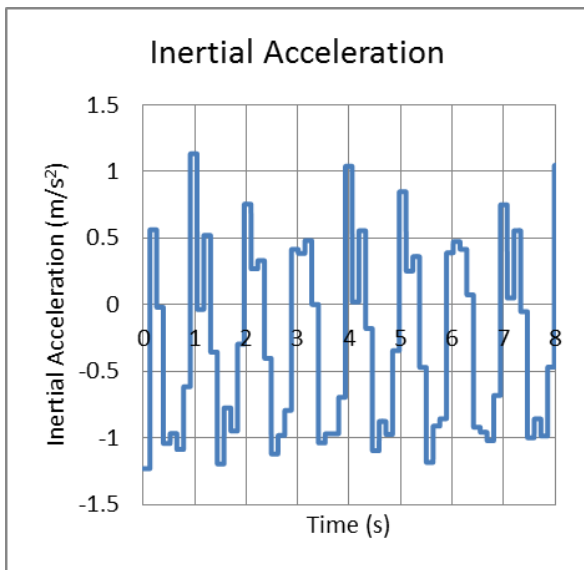
The dynamic pressure comparison between CFD and experiment is done for fill levels 20%, 40% and 60% in linear, weakly nonlinear and nonlinear sloshing regimes.

5.4.2 Dynamic Pressure comparison between CFD and experiment for 20% Fill

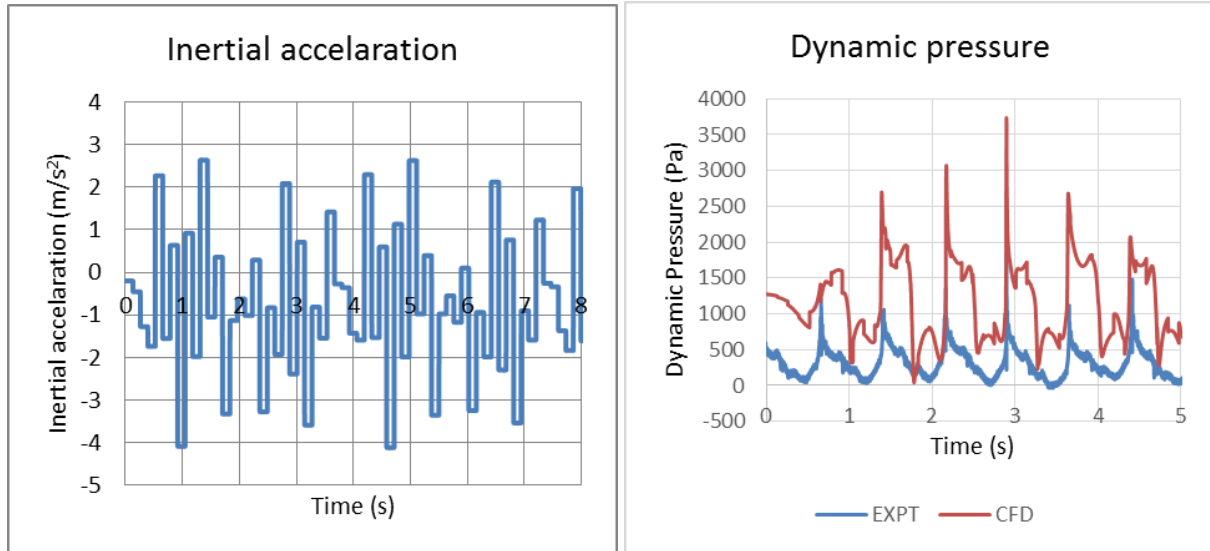
Figure 5.4.2 A, B and C represents the comparison of dynamic pressure between CFD and experiment for 20% fill level in linear, weakly nonlinear and nonlinear sloshing regimes. Plots of inertial acceleration from experiment and dynamic pressure for CFD and experiment is presented. All these comparisons are made pressure probes placed at a location of 10 percent below fill level as most of the dynamic activities are occurring at this location.



A: Fill level= 20%, Excitation Frequency= 0.5fs, Linear sloshing



B: Fill level= 20%, Excitation Frequency= 0.75fs, weakly nonlinear sloshing



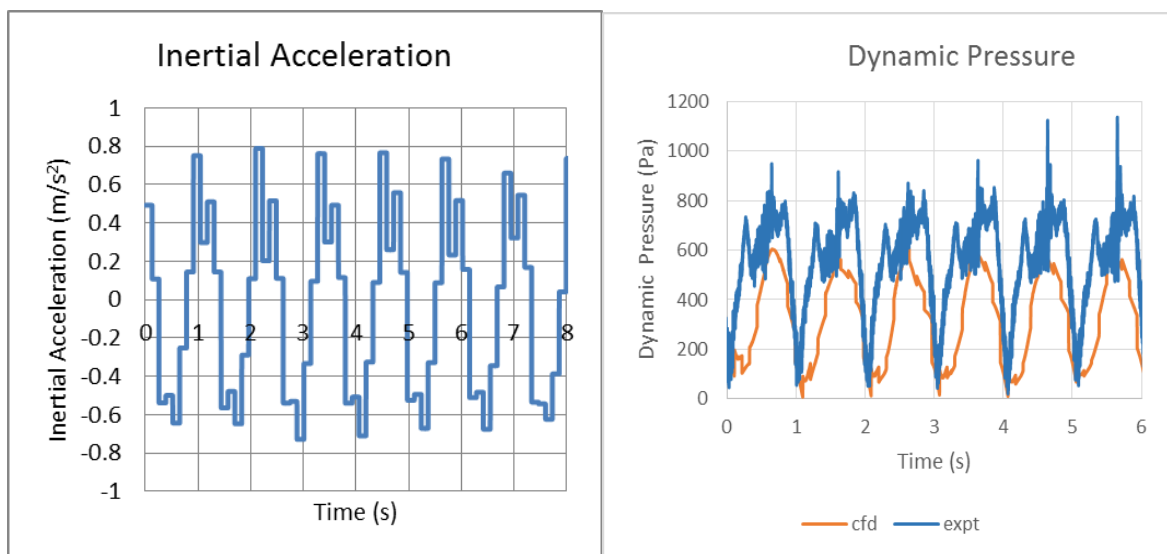
C: Fill level= 20%, Excitation Frequency= 1fs, nonlinear sloshing

Figure 5.4.2: Dynamic Pressure comparison between CFD and experiment for 20% fill

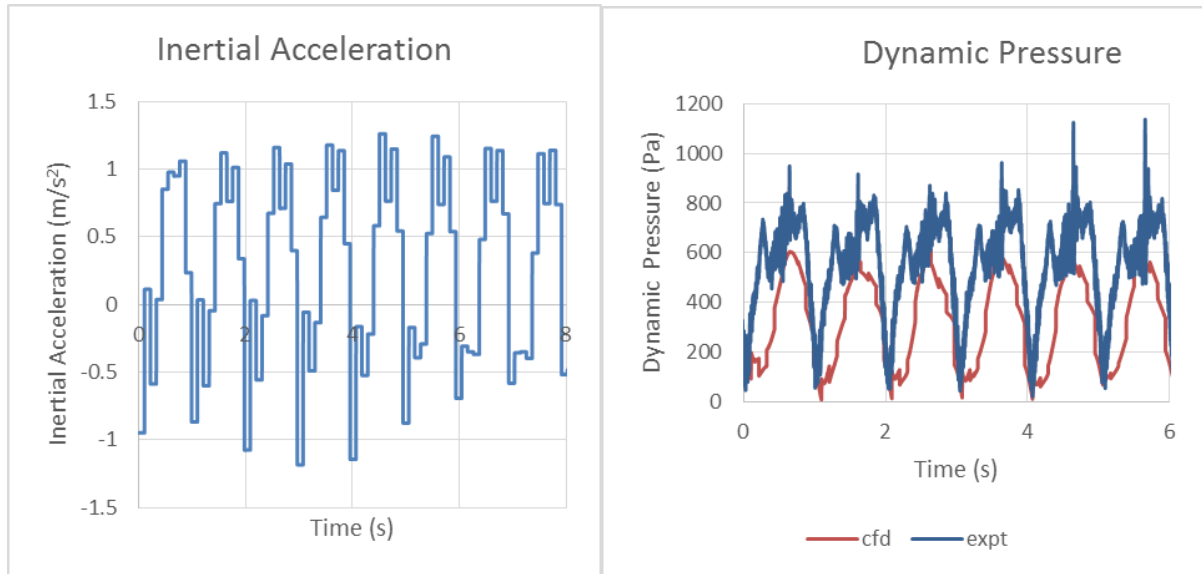
Cycle to cycle variation is seen in inertial acceleration and dynamic pressure plots and trend is same in inertial acceleration and experimental dynamic pressure plot. Events are occurring at the same time as seen from inertial acceleration, CFD dynamic pressure and experimental dynamic pressure plot. So data is synchronous. There is discrepancy in pressure data from CFD and experiment as working range of the pressure sensors used in experiment is high compared to sloshing pressures. It is difficult to define whether we are working within the uncertainty of experimental measurements as cycle to cycle variation is large in dynamic pressure plots. It can be seen from dynamic pressure plots, secondary peak is not well defined in CFD when compared to experiment. Dynamic pressure values are higher for nonlinear sloshing compared to linear sloshing which is in agreement with the literature.

5.4.3 Dynamic Pressure comparison between CFD and experiment for 40% Fill

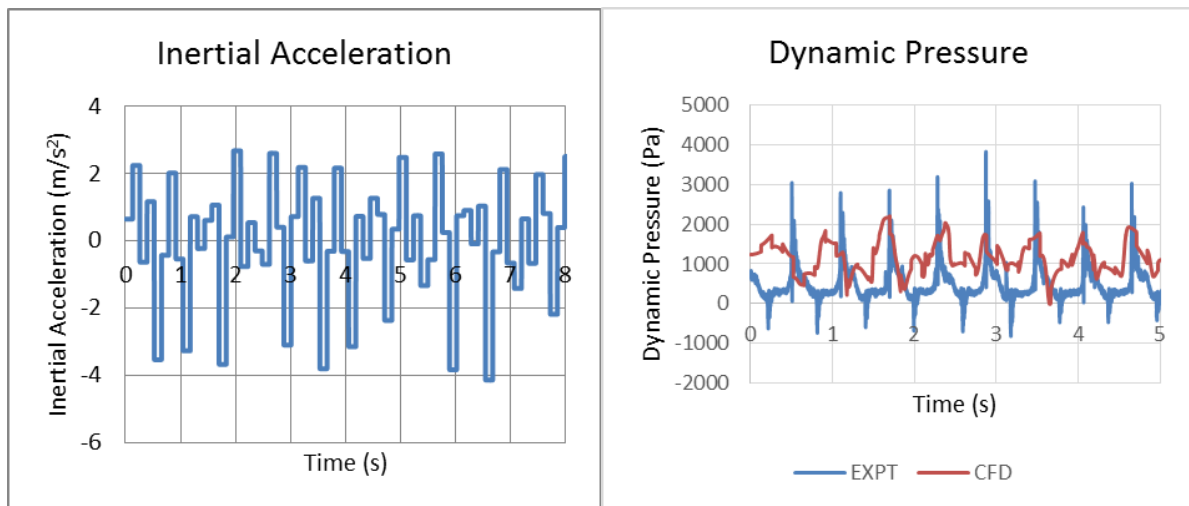
Figure 5.4.3 A, B and C represents the comparison of dynamic pressure between CFD and experiment for 40% fill level in linear, weakly nonlinear and nonlinear sloshing regimes. Plots of inertial acceleration from experiment and dynamic pressure for CFD and experiment is presented. All these comparisons are made pressure probes placed at a location of 10 percent below fill level as most of the dynamic activities are occurring at this location.



A: Fill level= 40%, Excitation Frequency= 0.5fs, Linear sloshing



B: Fill level= 40%, Excitation Frequency= 0.6fs, weakly nonlinear sloshing



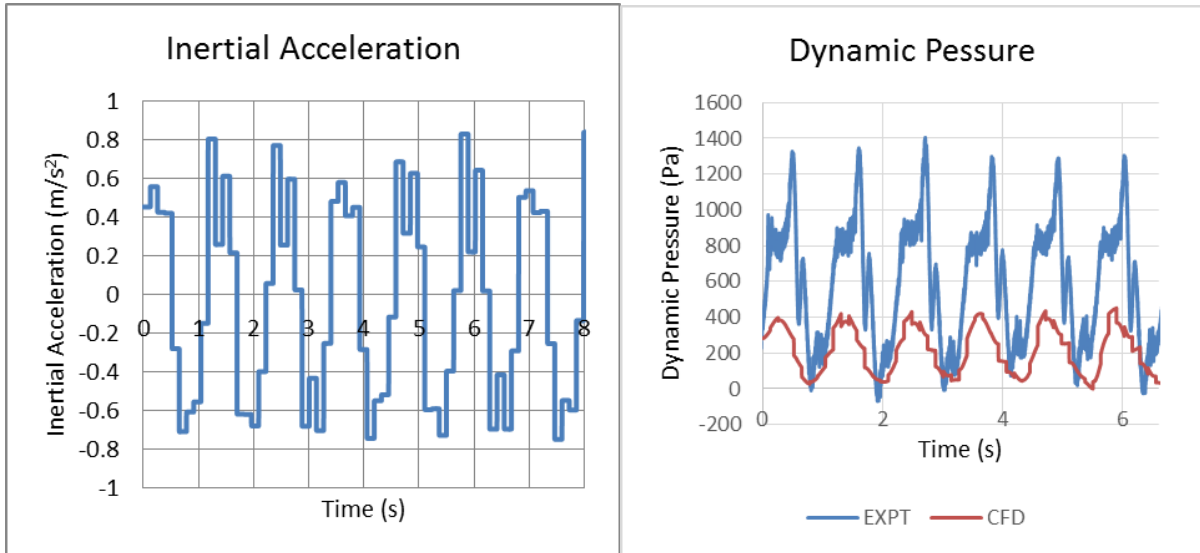
C: Fill level= 40%, Excitation Frequency= 1fs, nonlinear sloshing

Figure 5.4.3: Dynamic Pressure comparison between CFD and experiment for 40% fill

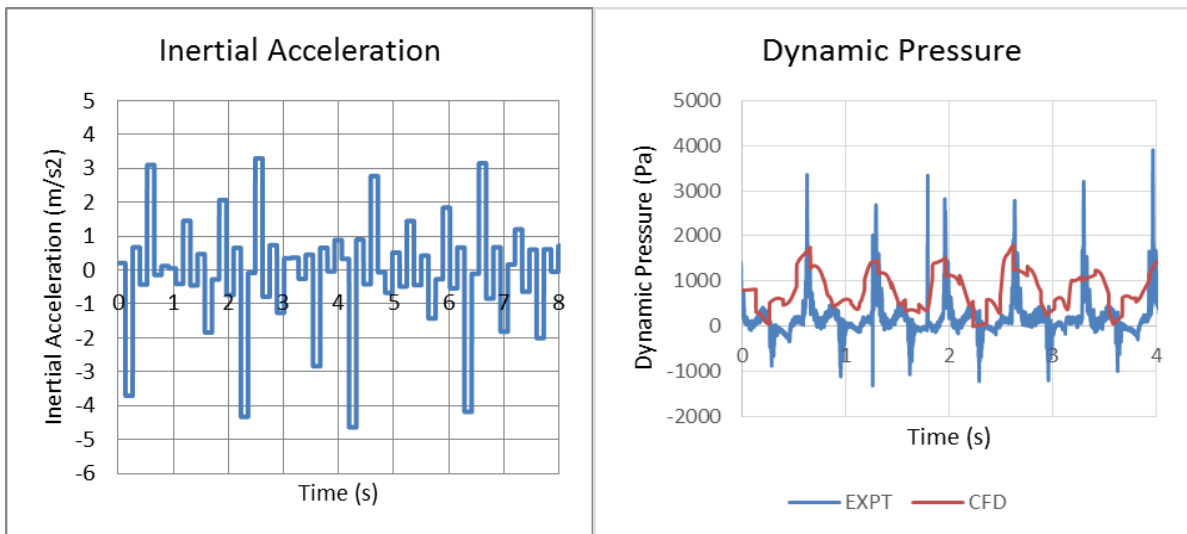
Events are occurring at the same time as seen from inertial acceleration, CFD dynamic pressure and experimental dynamic pressure plot. So data is synchronous. There is discrepancy in pressure data from CFD and experiment as working range of the pressure sensors used in experiment is high compared to sloshing pressures. Cycle to cycle variation is not large compared to 20% fill level in dynamic pressure plots. CFD and experimental dynamic pressure matches well in linear sloshing regime as seen from Figure 5.4.3 A. In figure 5.4.3 B, in weakly nonlinear sloshing regime, it is found that the difference between CFD and experimental dynamic pressure is approximately 200 Pa which states that we are working within the uncertainty for weakly nonlinear regime. Similarly from figure 5.4.3 C, in nonlinear sloshing regime, it is found that the difference between CFD and experimental dynamic pressure is approximately 1000 Pa which is well within the uncertainty in the experimental pressure measurements in weakly nonlinear regime. It can be seen from dynamic pressure plots, secondary peak is not well defined in CFD when compared to experiment. Dynamic pressure values are higher for nonlinear sloshing compared to linear sloshing which is in agreement with the literature.

5.4.4 Dynamic Pressure comparison between CFD and experiment for 40% Fill

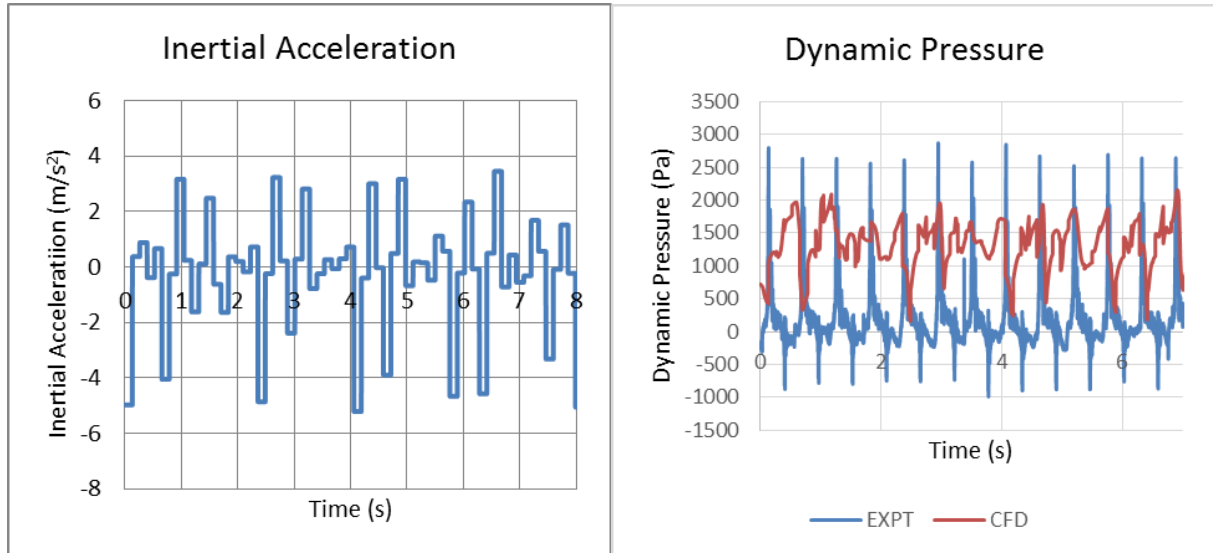
Figure 5.4.4 A, B and C represents the comparison of dynamic pressure between CFD and experiment for 60% fill level in linear, weakly nonlinear and nonlinear sloshing regimes. Plots of inertial acceleration from experiment and dynamic pressure for CFD and experiment is presented. All these comparisons are made pressure probes placed at a location of 10 percent below fill level as most of the dynamic activities are occurring at this location.



A: Fill level= 60%, Excitation Frequency= 0.5fs, Linear sloshing



B: Fill level= 60%, Excitation Frequency= 0.85fs, weakly nonlinear sloshing



C: Fill level= 60%, Excitation Frequency= 1fs, nonlinear sloshing

Figure 5.4.4: Dynamic Pressure comparison between CFD and experiment for 60% fill

Events are occurring at the same time as seen from inertial acceleration, CFD dynamic pressure and experimental dynamic pressure plot. So data is synchronous. There is discrepancy in pressure data from CFD and experiment as working range of the pressure sensors used in experiment is high compared to sloshing pressures. There is discrepancy CFD and experimental dynamic pressure in linear sloshing regime as seen from Figure 5.4.4 A. In figure 5.4.4 B, in weakly nonlinear sloshing regime, it is found that the difference between CFD and experimental dynamic pressure is approximately 500 Pa which states that we are working within the uncertainty for weakly nonlinear regime. Similarly from figure 5.4.4 C, in nonlinear sloshing regime, it is found that the difference between CFD and experimental dynamic pressure is approximately 500 Pa which is well within the uncertainty in the experimental pressure measurements in weakly nonlinear regime. It can be seen from dynamic pressure plots, secondary peak is not well defined in CFD when compared to experiment. Dynamic pressure values are higher for nonlinear sloshing compared to linear sloshing which is in agreement with the literature.

5.5 PIV Analysis

Particle Image velocimetry is a technique used to get velocity contours in the entire flow region. The following study presents the results of comparison of velocity contours from CFD and PIV for 40% fill in linear and weakly nonlinear sloshing regime. The procedure to calculate the velocity in both CFD and PIV is explained in figure 5.5.1.

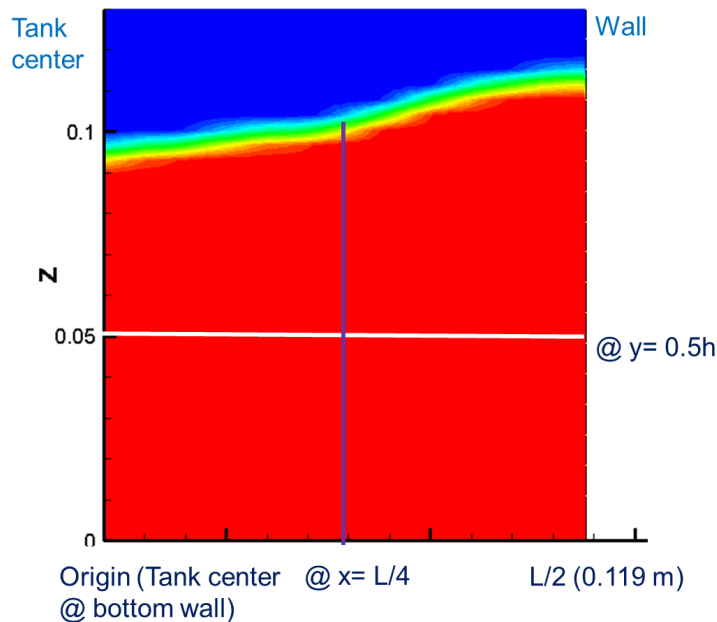


Figure 5.5.1: Procedure to calculate velocity in CFD and PIV

Figure 5.5.1 shows the procedure to calculate velocity in CFD and PIV in which only half section of the tank is considered from center of tank to wall. Non dimensional velocity is plotted against non-dimensional distance. Velocity is non-dimensionalized with tank velocity while distance is non-dimensionalized with fill level. Velocity vectors are plotted at predefined locations such as non-dimensional V-component of velocity is plotted against the non-dimensional longitudinal distance at 50% of the fill level. Similarly, non-dimensional U-component of velocity is plotted against the non-dimensional transverse distance at 50% of the longitudinal distance.

Non-dimensional parameters are:

$$U = U_{\text{avg}} / V_{\text{tank}} \quad ; \quad V = V_{\text{avg}} / V_{\text{tank}};$$

$$X = x / h \quad ; \quad Y = y / h$$

Where

V_{tank} – velocity of tank at a given crank angle

h - fill level

$U_{\text{avg}}, V_{\text{avg}}$ – Average value of velocity components over number of frames

5.5.1 Uncertainty in PIV measurements

Velocity in PIV measurement is calculated using the formula

$$v = \frac{\Delta x}{\Delta t}$$

where v = Velocity

Δx = Spot size (μm)

Δt = Time between two laser pulses (μs)

The uncertainty in velocity measurements is given by

$$u_v = \sqrt{\left[\left(\frac{\partial v}{\partial x} u_x \right)^2 + \left(\frac{\partial v}{\partial t} u_t \right)^2 \right]}$$

Where u_v, u_x, u_t are the uncertainties in velocity, displacement and time measurements.

Experimentally it is found that,

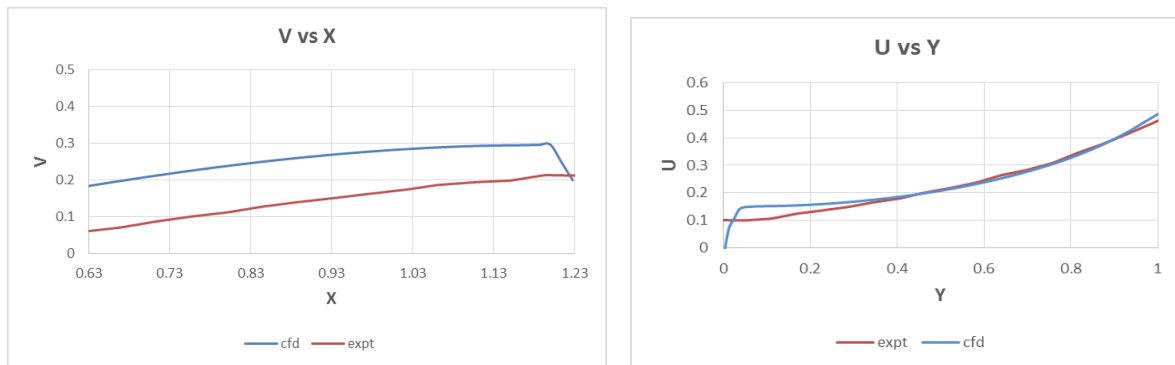
Uncertainty in Δx (u_x): 8.31 ± 0.415 mm

Uncertainty in Δt (u_t): 3 ± 0.5 ms

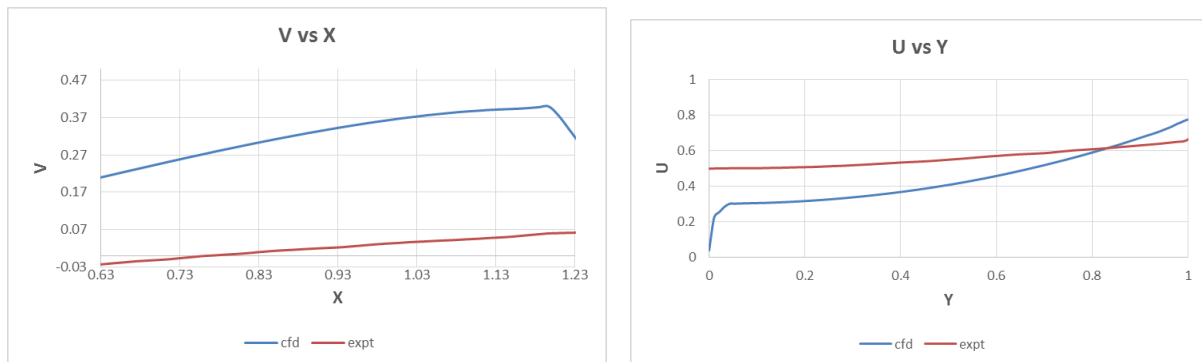
So, using the formula, Uncertainty in $v(u_v)$: 2.77 ± 0.482 m/s

5.5.2 Comparison of velocity components for CFD and PIV for 40% fill and 0.5fs

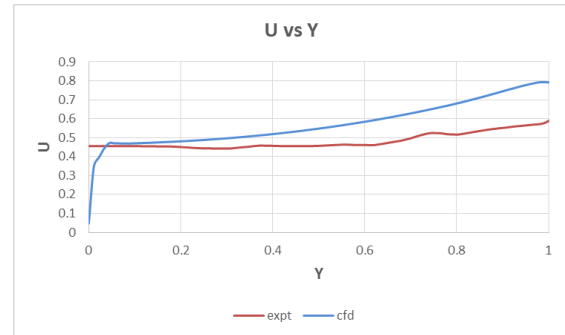
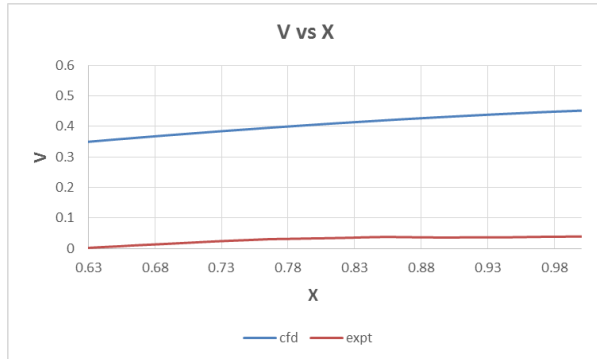
Figure 5.5.2 A, B, C, D represents the comparison of velocity components between CFD and PIV for 40% fill level in linear sloshing regimes. Plots of V vs X and U vs Y is presented for 90°, 135°, 225° and 270° from the TDC of the tank.



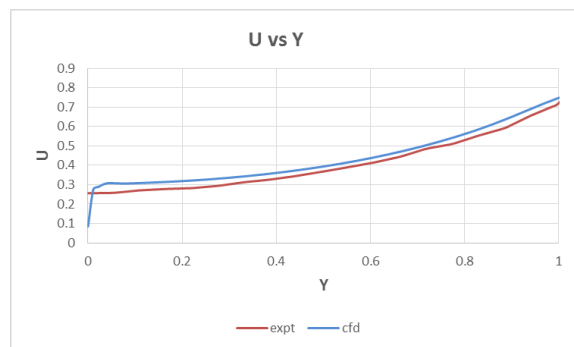
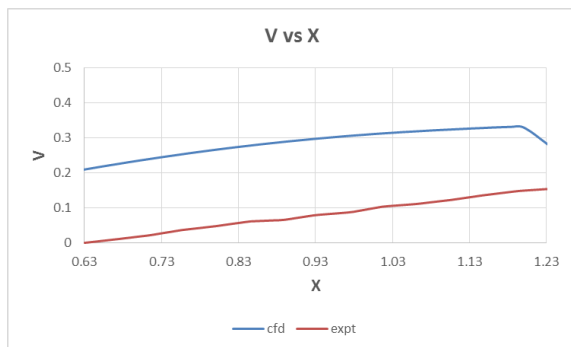
A: Comparison of velocity components for 40% fill level and 0.5fs (Linear sloshing Regime) at 90° crank angle



B: Comparison of velocity components for 40% fill level and 0.5fs (Linear sloshing Regime) at 135° crank angle



C: Comparison of velocity components for 40% fill level and 0.5fs (Linear sloshing Regime) at 225° crank angle



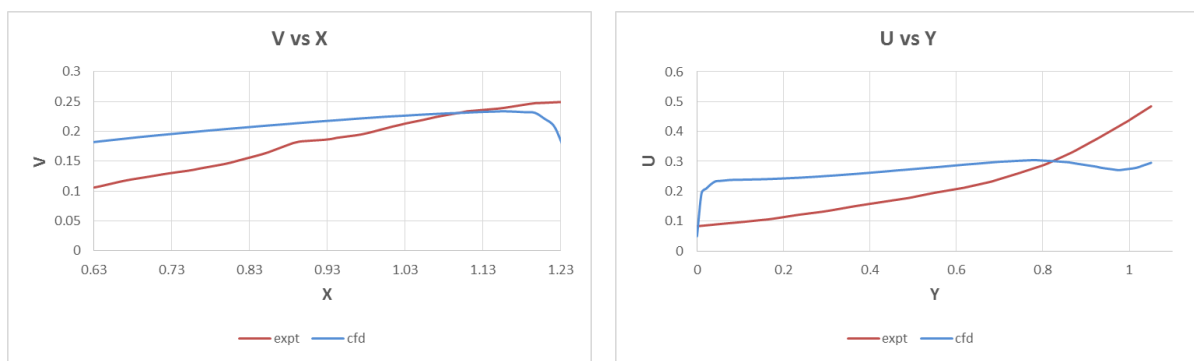
D: Comparison of velocity components for 40% fill level and 0.5fs (Linear sloshing Regime) at 270° crank angle

Figure 5.5.2 : Comparison of velocity components for 40% fill level and 0.5fs (Linear sloshing Regime) at various crank angle

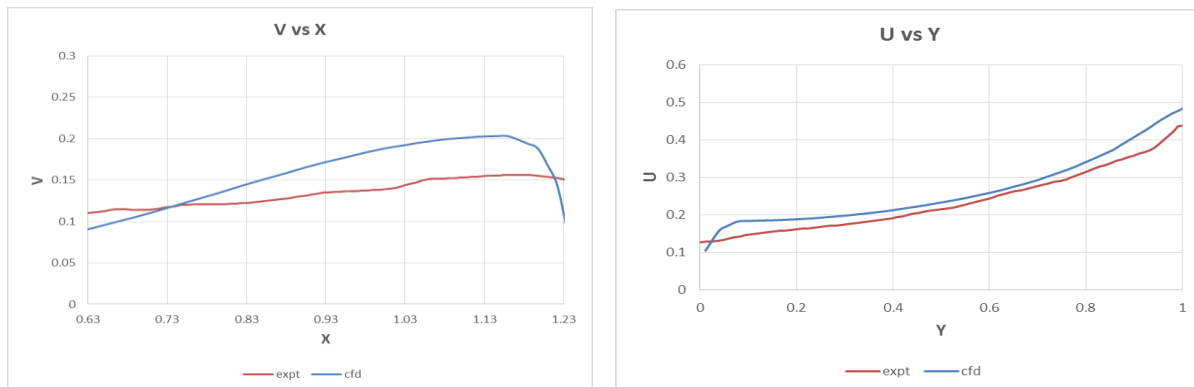
It can be clearly seen from figure 5.5.2 A,B,C,D that the as we move from center of the tank to wall, V-component of velocity increases. Also, as we go from bottom of the tank to interface, U-component of velocity increases. It is also seen that flow component of velocity matches well in CFD and PIV as compared to transverse component of velocity due to the fact that the turbulence models currently used predicts flow component of velocity.

5.5.3 Comparison of velocity components for CFD and PIV for 40% fill and 0.6 fs

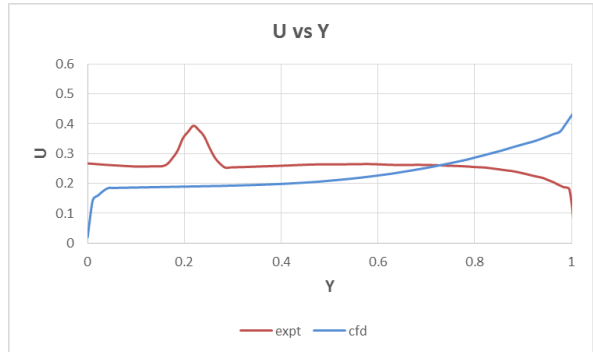
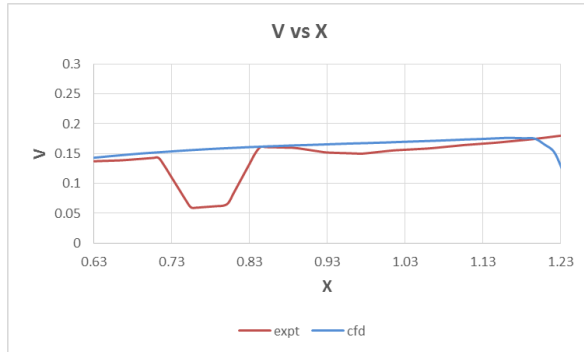
Figure 5.5.3 A, B, C, D represents the comparison of velocity components between CFD and PIV for 40% fill level in weakly nonlinear sloshing regimes. Plots of V vs X and U vs Y is presented for 90°, 135°, 225° and 270° from the TDC of the tank.



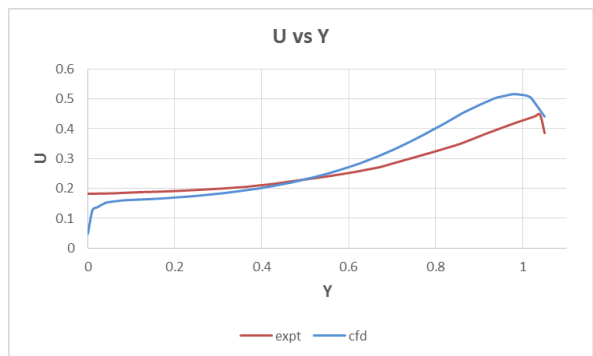
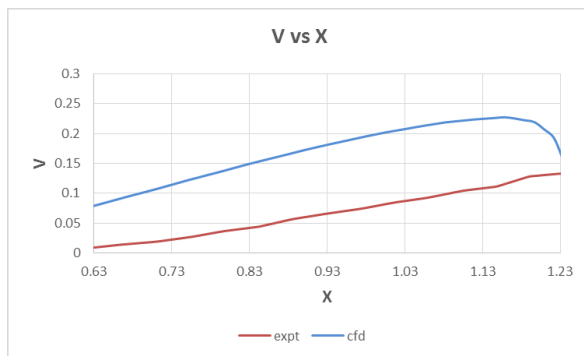
A: Comparison of velocity components for 40% fill level and 0.6fs (weakly nonlinear sloshing Regime) at 90° crank angle



B: Comparison of velocity components for 40% fill level and 0.6fs (weakly nonlinear sloshing Regime) at 135° crank angle



C: Comparison of velocity components for 40% fill level and 0.6fs (weakly nonlinear sloshing Regime) at 225° crank angle



D: Comparison of velocity components for 40% fill level and 0.6fs (weakly nonlinear sloshing Regime) at 270° crank angle

It can be clearly seen from figure 5.5.3 A,B,C,D that the as we move from center of the tank to wall, V-component of velocity increases. Also, as we go from bottom of the tank to interface, U-component of velocity increases. In figure C, there is sharp trough in PIV measurement which is due to bad vector in PIV measurement. It is also seen that flow component of velocity matches well in CFD and PIV as compared to transverse component of velocity due to the fact that the turbulence models currently used predicts flow component of velocity.

Chapter 6

Conclusion and Future Work

Experimental setup for Reciprocating Test rig has been developed for study of sloshing phenomenon under controlled loading condition. It is seen that events are occurring at the same time as seen from inertial acceleration, dynamic pressure and dynamic force plot. So data is synchronous. Cycle to cycle variation is seen in all the plots due to nonlinearity of fluid motion inside the tank. As we move from linear sloshing regime to nonlinear sloshing regime, dynamic pressure and dynamic force increases. Mesh independence study is done on uniform mesh and mesh size of $64*64*64$ is used for further analysis. A study is performed to evaluate different turbulence models and standard k- ϵ model is opted for numerical analysis.

In order to validate the CFD model, VOF wave height captured for simulation were compared with high speed camera images recorded during experimentation. It is found that the interface in CFD in HS video matches well in linear sloshing regime and which is well within the uncertainty in CFD wave height measurement in weakly nonlinear sloshing regime. Cycle to cycle variation is seen in inertial acceleration and dynamic pressure plots and trend is same in inertial acceleration and experimental dynamic pressure plot. Events are occurring at the same time as seen from inertial acceleration, CFD dynamic pressure and experimental dynamic pressure plot. So data is synchronous. There is discrepancy in pressure data from CFD and experiment as working range of the pressure sensors used in experiment is high compared to sloshing pressures. Dynamic pressure values are higher for nonlinear sloshing compared to linear sloshing which is in agreement with the literature.

PIV analysis shows that as we move from center of the tank to wall, V-component of velocity increases. Also, as we go from bottom of the tank to interface, U-component of velocity increases. It is also seen that flow component of velocity matches well in CFD and PIV as compared to transverse component of velocity due to the fact that the turbulence models currently used predicts flow component of velocity.

Future Work

1. Numerical methodology to study sloshing phenomenon in non-linear regime has to be developed and validated. This includes use of mesh refinement.
2. For PIV, better turbulence model needs to be developed so as to predict transverse component of velocity well.
3. A CAE based methodology to study splash phenomenon needs to be developed
4. Study of sloshing in tanks with different aspect ratios and in actual automotive fuel tank needs to be performed.
5. Development of an analytical model which compares well with numerical and experimental methodology.

References

- [1] K. P. Thiagarajan, D. Rakshit, and N. Repalle, “The air–water sloshing problem: Fundamental analysis and parametric studies on excitation and fill levels,” *Ocean Eng.*, vol. 38, no. 2, pp. 498–508, 2011.
- [2] C. Wachowski, J. W. Biermann, and R. Schala, “Approaches to analyse and predict slosh noise of vehicle fuel tanks.”
- [3] S. aus der Wiesche. Noise due to sloshing within automotive fuel tanks. *Forschung im Ingenieurwesen* 70, (2005) 13–24.
- [4] V. V. S. Vytla and Y. Ando, “Fluid Structure Interaction Simulation of Fuel Tank Sloshing,” *Optimization*, vol. 2013, pp. 01–09.
- [5] M. Perić and T. Zorn, “Simulation of sloshing loads on moving tanks,” in *ASME 2005 24th International Conference on Offshore Mechanics and Arctic Engineering*, 2005, pp. 1017–1026.
- [6] M. Hattori, A. Arami, and T. Yui. Wave impact pressure on vertical walls under breaking waves of various types. *Coastal Engineering* 22, (1994) 79–114.
- [7] Raouf A. Ibrahim, “Liquid Sloshing Dynamics-Theory and Applications.”
- [8] L. Khezzar, A. Seibi, and A. Goharzadeh, “Water Sloshing in Rectangular Tanks—An Experimental Investigation & Numerical Simulation,” *Int J Engineering IJE*, vol. 3, no. 2, pp. 174–184, 2009.
- [9] H. Rezaei and M. J. Ketabdari, “Numerical Modelling of Sloshing with VOF Method,” 2007
- [10] M. Hinatsu, Y. Tsukada, R. Fukasava, and Y. Tanaka, “Experiments of two-phase flows for the joint research,” in *Proc. SRI-TUHH mini-Workshop on Numerical Simulation of Two-Phase Flows*, Ship Research Institute, Tokyo, 2001.
- [11] C. Lugni, M. Brocchini, and O. M. Faltinsen, “Wave impact loads: The role of the flip-through,” *Phys. Fluids 1994-Present*, vol. 18, no. 12, p. 122101, 2006.

[12] R Banerjee and K M Isaac “Evaluation of turbulence closure scheme for stratified two phase flow”, Proceedings of IMECE ‘03, 2003 ASME International Mechanical Engineering Congress and Exposition

[13] Jadon V., “Numerical & Experimental Study of Sloshing of Liquid in a Rectangular Tank”, Master’s Thesis, IIT Hyderabad

[14] Agawane G., “Prediction of sloshing noise in a Rectangular Tank”, Master’s Thesis, IIT Hyderabad

[15] U. CD-adapco, GUIDE: STAR-CCM+. Version, 2009.

[16] User Guide, INSIGHT 4G